JOURNAL OF GEOPHYSICAL RESEARCH, VOL. 91, NO. B6, PAGES 6441-6464, MAY 10, 1986

Synthetic Seismograms From Coupled Free Oscillations: Effects of Lateral Structure and Rotation

JEFFREY PARK[1]

Institute of Geophysics and Planetary Physics, Scripps Institution of Oceanography, University of California, San Diego, La Jolla

Synthetic seismograms from coupled free oscillations are calculated for a regionalized continent-ocean model of the upper mantle and a recently proposed spherical harmonic lateral structure model. Spectral correlation analysis of these synthetic records, containing Rayleigh waves with period $T \gtrsim 160$ s, reveals the size of departures from the assumption that the waveform perturbation can be explained by just the structure under the great circle between source and receiver. Arrival azimuth deflections of up to 10° are observed on horizontal synthetics using a 2.3% variation in shear velocity between continents and oceans. Among the M84A synthetics, the great circle travel times R_3-R_1, R_4-R_2, R_5-R_3 vary on average by 3–5 s for $3 \lesssim f \lesssim 6$ mHz surface wave motion. Comparison between synthetics, calculated to be sensitive to even-order structure or to both even- and odd-order structure, gives a 5-s average time delay attributable to odd-order structure. Significant Rayleigh wave packet amplitude anomalies are common in the synthetic records and are nearly as common in synthetics calculated for the even-order structure as in those sensitive to all structure. Examples suggest that model M84A does not consistently reproduce the amplitude anomalies observed in International Deployment of Accelerometers (IDA) and Global Digital Seismographic Network (GDSN) data. Lastly, we demonstrate the effect of Coriolis coupling in the time domain. Visible precursors to Rayleigh wave packets are predicted in cases of favorable source-receiver geometry. These precursors are caused by the spheroidal component of the hybrid, predominantly toroidal, low-frequency ($f \lesssim 4.2$ mHz) Love wave, whose arrival precedes that of the Rayleigh wave. We present examples of this anomalous waveform in IDA data from a large strike-slip earthquake in New Guinea, showing a qualitative fit to the coupled-mode prediction.

1. INTRODUCTION AND METHODS

Coupled-mode calculations, in principle, offer a more accurate method of determining the earth's response to seismic sources than techniques that rely on asymptotic or high-frequency forms of the equations of motion, e.g., surface wave tomography [*Nakanishi and Anderson*, 1983, 1984; *Woodhouse and Dziewonski*, 1984; *Tanimoto and Anderson*, 1985] or generalized ray techniques. For response at frequencies below a chosen cutoff frequency ω_{cutoff}, a seismogram can be represented as a finite sum of elastic-gravitational free oscillations. Nominally second-order effects such as Coriolis coupling between spheroidal and toroidal modes are accounted for naturally by the coupled-mode formalism. There are additional second-order effects when seismic particle motion on an earth model with aspherical boundaries is expressed in terms of functions that satisfy spherical boundary conditions. These latter effects are not accounted for. In addition, approximations must always be made in order for the coupled-mode calculations to remain numerically tractable. The errors induced by the second type of approximation are relatively easy to assess. One can test directly the effects of breaking a large coupling matrix into smaller blocks or else use theorems from numerical linear algebra to do so. In an asymptotic technique one might need to construct a new theory to account for a breakdown of initial assumptions. In surface wave tomography, the perturbation of waveforms is calculated under the assumption that wave energy travels only along the great circle path connecting the source and receiver. As a test of this assumption one can calculate ray paths on an earth model with lateral structure [*Wong and Woodhouse*, 1983; *Lay and Kanamori*, 1985], but this improvement still omits the significant off-path scattering shown in the spherical-surface sampling kernels of *Woodhouse and Girnius* [1982]. The increase in computational resources required by coupled-mode calculations limits their general use at this time. Improvements in computational facilities, in particular the imminent arrival of the second generation of Cray-like supercomputers (e.g., the Cray XMP, Cray 2, the Hitachi S-810, the ETA GF-10, the Fujitsu VP-200) will increase the feasibility of the calculations in the near future. The purpose of coupled-mode synthetic seismograms at this time is twofold. Such calculations can be used as a check on the validity of approximations to the full equations of motion that have been used as inspirations for inversion schemes [e.g., *Jordan*, 1978; *Dahlen*, 1979; *Woodhouse and Girnius*, 1982] and as a probe to discover new waveform phenomena.

This study considers coupling principally between free oscillation multiplets and their component singlets in the fundamental mode dispersion branches ${}_0S_l$, ${}_0T_l$, corresponding to fundamental Rayleigh and Love waves, respectively. We compare several recipes for coupling ${}_0S_l$, ${}_0T_l$ modes in order to assess the relative importance of specified effects of lateral structure and rotation. We first demonstrate in section 2 the wave packet phase shift and refraction effects using a simple continent ocean model. Surface wave amplitude anomalies due to focusing and defocusing through structure are demonstrated and com-

---

[1] Now at Geophysical Fluid Dynamics Program, Princeton University, Princeton, New Jersey.

Paper number 5B5569.
0148-0227/86/005B-5569$05.00

pared in section 3 with a small set of data examples. The coupling of spheroidal and toroidal fundamentals through both Coriolis force and structure, which caused the subsidiary spectral peaks noted by *Masters et al.* [1983*a*], causes anomalous wave packet arrivals in the time domain. The geometric dependence of this effect and its occurrence in low-frequency data are discussed in section 4.

Three coupling recipes and a control calculation are compared. The control is the spherical earth approximation, in which no splitting or coupling occurs and all singlets within the multiplets ${}_0S_l$ share the degenerate multiplet frequency. The first coupling recipe will be "first-order splitting" of singlets within distinct ${}_0S_l$ multiplets, calculated by means of degenerate perturbation theory. First-order splitting does not include interactions between free oscillation multiplets. First-order splitting of degenerate multiplets is sensitive only to even-order structure. First-order splitting shares this restriction with great circle surface wave studies and asymptotic multiplet peak shift theory but is more general as it includes the effects of off-path scattering. A further step in complexity is taken in the second recipe in which fundamental mode multiplets ${}_0S_l$ are allowed to couple with neighboring fundamental modes of like type. Since neighboring modes on the dispersion branch differ by one in angular order, these ${}_0S_{l-1} - {}_0S_l - {}_0S_{l+1}$ calculations show the effects of odd-angular order structure. Although coupling extends to all modes along the dispersion branch and to overtones as well, the dominant contribution by long-wavelength odd-order lateral structure to the Rayleigh waveform should be governed by coupling according to this recipe. One must go to ${}_0S_{l\pm 3}$ to obtain further same-branch coupling partners sensitive to odd-order structure. Since the increase in degenerate multiplet frequency ${}_0\omega_l^S$ is roughly linear in l, the effects of coupling to ${}_0S_{l\pm 3}$ are reduced by roughly 1/3 in amplitude and 1/9 in frequency relative to those due to ${}_0S_{l\pm 1}$ coupling. Odd-order-sensitive coupling to overtones and toroidal fundamentals is isolated to fundamentals ${}_0S_l$ that possess a convenient coupling partner, e.g., ${}_0S_{26} - {}_0T_{26}$. The radial and angular dependence of particle motion for the modes ${}_0S_l$, ${}_0S_{l\pm 1}$ are quite similar as $l \gtrsim 10$, so that coupling through simple, long-wavelength lateral structures is relatively more efficient. The particle motion for fundamental/overtone, or spheroidal/toroidal coupling pairs, is often quite dissimilar. It is shown by *Park* [1985] that such coupling becomes efficient only at structural angular orders $s \geqslant 10$. Given the disparities of radial functions and an irregular distribution of prospective fundamental/overtone, spheroidal/toroidal coupling pairs, one might expect same-branch coupling to exert a more coherent influence on the overall waveform. Same-branch coupling calculations contain all information pertaining to the refraction of surface waveforms on a generally heterogeneous earth. They provide a useful check on approximation schemes for calculating global surface wave response and on the bias of measured surface wave data used in global structural inversions.

We used a Galerkin procedure to calculate the coupling of spheroidal earth free oscillation singlets on an attenuative earth model with our chosen lateral structure model. If the effects on coupling due to dissimilar attenuation rates could be neglected, a variational formalism was used which required less computation. The two computational approaches are derived in a similar manner. On a nonrotating spherical earth model the equations of motion for small seismic oscillations about an equilibrium state can be solved in terms of vector spherical harmonics. One expresses $\mathbf{s}(\mathbf{r}) = \mathbf{s}(r,\theta,\phi)$

$$\mathbf{s} = {}_nU_l(r)\hat{\mathbf{r}}\,Y_l^m(\theta,\phi) + {}_nV_l(r)\nabla_1 Y_l^m(\theta,\phi) - {}_nW_l(r)\hat{\mathbf{r}} \times \nabla_1 Y_l^m(\theta,\phi) \qquad (1)$$

where $\hat{\mathbf{r}}$, $\hat{\theta}$, $\hat{\phi}$ are unit vectors in the spherical coordinate directions, $\nabla_1 = \hat{\theta}\partial_\theta + \operatorname{cosec}\theta\hat{\phi}\partial_\phi$ is the spherical surface gradient and $Y_l^m(\theta,\phi)$ are scalar spherical harmonics of angular order l and azimuthal order m. The subscript n refers to overtone number. We use the definition of *Edmonds* [1960], for which the spherical harmonics are normalized by

$$\int_0^{2\pi}\int_0^{\pi} [Y_{l'}^{m'}(\theta,\phi)]^* Y_l^m(\theta,\phi)\sin\theta\, d\theta\, d\phi = \delta_{mm'}\delta_{ll'} \qquad (2)$$

where integration is over the unit sphere. If $\mathbf{s}$ is a toroidal mode, ${}_nU_l(r) = {}_nV_l(r) = 0$. If $\mathbf{s}$ is a spheroidal mode ${}_nW_l(r) = 0$. Spheroidal deformation fields have an associated gravitational perturbation ϕ_1, which we leave implicit in the notation. On a spherical nonrotating earth model, each overtone number/angular order pair (n,l) defines a multiplet within which the $2l+1$ azimuthal orders $m = -l, -l+1, \ldots, l-1, l$ label individual singlets. Each singlet represents a possible angular pattern of motion at the degenerate multiplet frequency ${}_n\omega_l$. We will restrict attention to fundamental $(n = 0)$ modes in this study.

The formal aspects of the normal mode variational principle have been developed by *Dahlen* [1973], *Luh* [1974], *Woodhouse* [1976], *Woodhouse and Dahlen* [1978], and *Woodhouse* [1980], among others. *Dahlen* [1981] considered the effects of modal attenuation on coupling but restricted attention to the splitting of isolated degenerate multiplets. *Tanimoto and Bolt* [1983] recognized the need for a Galerkin formalism in their theoretical study of coupling between toroidal modes. Attenuative effects on coupling were shown to be observable by *Masters et al.* [1983*a*]. Formulas for calculating synthetic seismograms from coupled-mode oscillations are developed by *Park and Gilbert* [1986], from which the following computational recipes have been culled.

A variational principle can be obtained from the equations of motion for $\mathbf{s}$ by dotting both sides of the equation by $D_t\mathbf{s}^*$, where D_t is the substantial (Lagrangian) time derivative and $\mathbf{s}^*$ is the complex conjugate of $\mathbf{s}$. One integrates the resulting scalar quantity over the earth's volume V to obtain an expression for the Lagrangian of the system governed by Hamilton's variational principle. It is convenient to rearrange the integral functionals by powers of ω.

$$L = V(\mathbf{s}^*,\mathbf{s}) + \omega W(\mathbf{s}^*,\mathbf{s}) - \omega^2 T(\mathbf{s}^*,\mathbf{s}) \qquad (3)$$

where we have left implicit the dependence on ϕ_1 in the notation of the functionals.

$$T(\mathbf{s}^*,\mathbf{s}) = \int_V \rho\,\mathbf{s}^*\cdot\mathbf{s}\,dV \qquad (4)$$

$$W(\mathbf{s}^*,\mathbf{s}) = \int_V 2i\rho\mathbf{s}^* \cdot (\mathbf{\Omega} \times \mathbf{s})dV \tag{5}$$

$$V(\mathbf{s}^*,\mathbf{s}) = \int_V [\rho(\mathbf{s}^* \cdot \nabla\phi_1 + \mathbf{s} \cdot \nabla\phi_1^* + \mathbf{s}^* \cdot \nabla\nabla\Phi \cdot \mathbf{s}) + \frac{1}{4\pi G} |\nabla\phi_1|^2 + \boldsymbol{\epsilon}^* : \mathbf{\Lambda} : \boldsymbol{\epsilon}]dV + \int_\Sigma [\tilde{\mathbf{M}}(\mathbf{s}^*,\mathbf{s})]_-^+ d\Sigma \tag{6}$$

are the kinetic energy functional, Coriolis functional, and potential energy functional, respectively. In the equation, $\mathbf{\Omega}$ is the earth's rotation vector, G is the gravitational constant, Λ_{ijkl} is the tensor relating stress and strain in a prestressed medium, and $\boldsymbol{\epsilon} = ½(\nabla\mathbf{s} + (\nabla\mathbf{s})^T)$ is the strain associated with displacement $\mathbf{s}$. The surface integral

$$\tilde{\mathrm{M}} = ½[(\hat{\mathbf{n}} \cdot \mathbf{s}^*)\nabla_\Sigma \cdot (\pi_0\mathbf{s}) + (\hat{\mathbf{n}} \cdot \mathbf{s})\nabla_\Sigma \cdot (\pi_0\mathbf{s}^*) - \pi_0\mathbf{s}^* \cdot (\nabla_\Sigma\mathbf{s}) \cdot \hat{\mathbf{n}} - \pi_0\mathbf{s} \cdot (\nabla_\Sigma\mathbf{s}^*) \cdot \hat{\mathbf{n}}] \tag{7}$$

arises from the extra prestress terms in (6) necessary at frictionless internal boundaries; π_0 is the normal stress at the boundary, and ∇_Σ is the vector surface gradient. $[\tilde{\mathrm{M}}]_-^+$ vanishes at welded boundaries and at the free surface, contributing to L only at fluid-solid boundaries. The variational principle is satisfied for an elastic-gravitational deformation field $(\mathbf{s},\phi_1)$ at a frequency ω if the functional L is stationary with respect to small perturbations in $\mathbf{s}$ and ϕ_1. Such deformation fields satisfy the equations of motion. The variational principle thus formulated becomes

$$L = 0 = V(\mathbf{s}^*,\mathbf{s}) + \omega W(\mathbf{s}^*,\mathbf{s}) - \omega^2 T(\mathbf{s}^*,\mathbf{s}) \tag{8}$$

and

$$\delta L = 0 \tag{9}$$

with respect to small perturbations in $\mathbf{s}$ and ϕ_1.

The development of the Galerkin formalism is identical up to this point. The variational and Galerkin treatments diverge in the behavior of the tensor $\mathbf{\Lambda}$ in (6), which relates incremental strain to incremental elastic energy. The fourth-order tensor $\{\Lambda_{ijkl}\}$ can be related to the elastic tensor $\{C_{ijkl}\}$ and the initial stress field $\{T_{ij}^0\}$:

$$\Lambda_{ijkl} = C_{ijkl} + ½(T_{ij}^0\delta_{kl} + T_{kl}^0\delta_{ij} + T_{ik}\delta_{jl} - T_{jk}^0\delta_{il} - T_{il}^0\delta_{jk} - T_{jl}^0\delta_{ik}) \tag{10}$$

with δ_{ij} the Kronecker delta. The C_{ijkl} depend on the various elastic constants (the Lamè parameters λ, μ if the medium is isotropic). The variational formalism requires the C_{ijkl} to be real valued and independent of frequency. The Galerkin formalism allows the C_{ijkl} to be both complex-valued (attenuative) and frequency-dependent (physically dispersive). The frequency dependence of the C_{ijkl} is related to its imaginary part through the Kramers-Kronig relations [*Minster*, 1978*a,b*; *Chin*, 1980]. *Park and Gilbert* [1986] found physical dispersion to have a negligible effect on typical coupling calculations with reasonable Q models. If the C_{ijkl} are real, $V(\mathbf{s}^*,\mathbf{s})$ is a Hermitian bilinear form (as are $W(\mathbf{s}^*,\mathbf{s})$ and $T(\mathbf{s}^*,\mathbf{s})$). If attenuation is modeled in the C_{ijkl}, $V(\mathbf{s}^*,\mathbf{s})$ loses this property.

In the numerical application of the variational principle, one selects a basis set of functions $\{\mathbf{s}_1,\mathbf{s}_2,\ldots,\mathbf{s}_N\}$, which have sufficient smoothness for the differential equation and also satisfy the spherical boundary conditions. One constructs an eigenfunction-eigenfrequency pair with a linear combination of the $\mathbf{s}_i$. Let $\mathbf{s} = \alpha_i\mathbf{s}_i$, with sum over i implicit. Substitution into (8) gives

$$0 = L = V(\alpha_i^*\mathbf{s}_i^*,\alpha_j\mathbf{s}_j) + \omega W(\alpha_i^*\mathbf{s}_i^*,\alpha_j\mathbf{s}_j) - \omega^2 T(\alpha_i^*\mathbf{s}_i^*,\alpha_j\mathbf{s}_j) = \alpha_i^*(V_{ij} + \omega W_{ij} - \omega^2 T_{ij})\alpha_j \tag{11}$$

where

$$\begin{aligned} V_{ij} &= V(\mathbf{s}_i^*,\mathbf{s}_j) \\ W_{ij} &= W(\mathbf{s}_i^*,\mathbf{s}_j) \\ T_{ij} &= T(\mathbf{s}_i^*,\mathbf{s}_j) \end{aligned} \tag{12}$$

are the matrix elements of interaction between the basis functions. If we define the N vector $\boldsymbol{\alpha} = (\alpha_1,\ldots,\alpha_N)$, and the interaction matrices $\mathbf{V} = \{V_{ij}\}$, etc., (11) reduces to

$$\boldsymbol{\alpha}^* \cdot (\mathbf{V} + \omega\mathbf{W} - \omega^2\mathbf{T}) \cdot \boldsymbol{\alpha} = 0 \tag{13}$$

Application of the variational principle gives us a quadratic problem in angular frequency ω. The quantity on the right side of (11) is stationary to small changes in $\boldsymbol{\alpha}$ if and only if $\boldsymbol{\alpha}$ is an eigenvector of $\mathbf{V} + \omega\mathbf{W} - \omega^2\mathbf{T}$. The matrices $\mathbf{V}$, $\mathbf{W}$, and $\mathbf{T}$ are all Hermitian, e.g., $V_{ij} = V_{ji}^*$, as they are projections of Hermitian forms. At the frequencies of interest in this study ($1\ \mathrm{mHz} < f < 6.2\ \mathrm{mHz}$) it is possible to reduce the matrix problem to a linear one by approximating $\omega W_{ij} \cong \hat{\omega}_{ij} W_{ij}$, where $\hat{\omega}_{ij}$ is a chosen frequency. We have taken $\hat{\omega}_{ij} = (\omega_{oi}\omega_{oj})^{½}$, the geometric mean of the degenerate frequencies of the ith and jth basis set singlets.

If attenuation is included, $\mathbf{V}$ is no longer Hermitian but general complex. This loss of symmetry alters the matrix eigenvalue problem in (13) to

$$\boldsymbol{\beta} \cdot (\mathbf{V} + \omega\mathbf{W} - \omega^2\mathbf{T}) \cdot \boldsymbol{\alpha} = 0 \tag{14}$$

where $\boldsymbol{\beta} \neq \boldsymbol{\alpha}^*$ in general. If (14) is solved for hybrid eigenfrequencies $\omega_1,\ldots,\omega_N$, the associated displacement eigenvectors $\boldsymbol{\alpha}_k$ are not orthogonal but still form a basis in complex N space as long as the matrix system is not defective; $\boldsymbol{\beta}_1,\ldots,\boldsymbol{\beta}_N$ form a basis dual to $\boldsymbol{\alpha}_1,\ldots,\boldsymbol{\alpha}_N$ so that $\boldsymbol{\beta}_k \cdot \boldsymbol{\alpha}_l = \delta_{kl}$. $\boldsymbol{\alpha}_k$ expresses the particle displacement of the kth hybrid singlet at the seismic receiver; $\boldsymbol{\beta}_k$ is used to calculate the source excitation of the kth singlet. If we use hybrid singlets $\tilde{\mathbf{s}}_k = \sum_{i=1}^{N} (\boldsymbol{\alpha}_k)_i\mathbf{s}_i$ from a coupling calculation to express the seismic response at position $\mathbf{r}$ due to a moment tensor source $\mathbf{M}(\omega)$ located at hypocenter $\mathbf{r}_0$, the particle motion $\mathbf{u}(\mathbf{r},\omega)$ is

$$\mathbf{u}(\mathbf{r},\omega) = \sum_{i=1}^{N}\sum_{j=1}^{N}\sum_{k=1}^{N} \alpha_{ki}\beta_{kj}\mathbf{s}_i(\mathbf{r})(\mathbf{M}(\omega) : \boldsymbol{\epsilon}_j^*(\mathbf{r}_0))C_k(\omega) \tag{15}$$

$C_k(\omega)$ is the resonance function of the kth hybrid singlet; $\boldsymbol{\epsilon}_j^*(\mathbf{r}_0)$ is the conjugated strain at $\mathbf{r}_0$ of the jth spherical earth singlet. If the variational coupling formalism is used, $\beta_{kj} = \alpha_{kj}^*$. A full time domain seismogram is synthesized by evaluating (15) for a series of decomposed coupling matrix systems (14) that extend over a chosen frequency band.

We have used the following procedure to include the effects of coupling of nearest neighbors on the fundamental spheroidal dispersion branch. Coupling matrices $\mathbf{V}$ and $\mathbf{T}$ are constructed using the $6l+3$ singlets of ${}_0S_{l-1}$, ${}_0S_l$, and

${}_0S_{l+1}$. For these multiplets the variation in Q is small as $l >> 1$, especially so when compared to the ~ 0.1 mHz real-part frequency spacing between multiplets. For this reason attenuation has been neglected in the interaction calculations, leaving $\mathbf{V}$ a Hermitian matrix. This approximation was tested for a sample case and found to be excellent, giving a factor of 3 increase in numerical speed. $\mathbf{V}-\omega^2\mathbf{T}$ for this recipe decomposes into hybrid singlets that group into three hybrid multiplets corresponding to ${}_0S_{l-1}$, ${}_0S_l$, and ${}_0S_{l+1}$. The coupling between adjacent ${}_0S_l$ was never, in the calculations that we performed, strong enough to disrupt the original configuration, i.e., three distinct groups of $2l-1$, $2l+1$, and $2l+3$ singlets well spaced in frequency. Since the complete nearest-neighbor coupling effects we desire are modeled only in the central hybrid multiplet, the outer hybrid multiplets are discarded, leaving a $(2l+1)$ by $(6l+3)$ complex-valued matrix of hybrid singlets and a $2l+1$ vector of hybrid eigenfrequencies. The real-valued hybrid eigenfrequencies are assigned the degenerate attenuation value of ${}_0S_l$ for the calculation of synthetic seismograms. We used this scheme for ${}_0S_l$, $3 \leqslant l \leqslant 55$, with ${}_0S_2-{}_0S_3$, ${}_0S_{55}-{}_0S_{56}$ coupling pairs to represent the end-members of the spheroidal branch up to $l=56$, $f \leqslant 6.2$ mHz; surface wave period $T > 160$ s.

The third coupling recipe considers the interaction of ${}_0S_l$ with ${}_0T_{l'}$, the closest toroidal fundamental mode. In general, $l-l'$ is not constant, due to the variable frequency spacing of nearest neighbors on the spheroidal and toroidal dispersion branches. At lowest frequencies, all modes ${}_0S_l$, $2 \leqslant l \leqslant 9$, ${}_0T_l$, $2 \leqslant l \leqslant 10$ were included in a single calculation, above which coupling pairs, e.g., ${}_0S_{10}-{}_0T_{11}$ were taken. Every change in $l-l'$ leaves one unmatched multiplet. ${}_0S_{24}$ was included with ${}_0S_{25}-{}_0T_{25}$ in order to model the expected strong Coriolis effect. Similarly, ${}_0S_{29}$ was included with ${}_0S_{28}-{}_0T_{28}$. At larger l where the angular order difference is too large for Coriolis coupling, the coupling of unpaired multiplets to neighboring multiplets was neglected. In this manner only first-order splitting was considered for ${}_0S_{35}$, ${}_0S_{40}$, ${}_0S_{46}$, and ${}_0S_{51}$. The full-complex Galerkin procedure was used, due to the disparity in Q between ${}_0S_l$, ${}_0T_{l'}$ modes. ${}_0S_{56}-{}_0T_{51}$ was the highest-frequency multiplet pair used. All hybrid singlets were retained for the construction of synthetic seismograms.

This coupling recipe is sensitive to even- or odd-order structure, respectively, depending on whether $l-l'$ is odd or even. The model 1066A dispersion branch crossings of ${}_0S_{37}-{}_0T_{35}$, ${}_0S_{43}-{}_0T_{40}$, ${}_0S_{48}-{}_0T_{44}$, ${}_0S_{54}-{}_0T_{49}$ are of particular interest. Coupling between Rayleigh and Love waves at $\omega > 4.2$ mHz is strongest at such crossings, due to the proximity in frequency of the coupling pairs. "Tears" in averaged multiplet frequency will occur here if the heterogeneity is strong enough. At $f \lesssim 4.2$ mHz, Coriolis coupling overshadows the coupling due to any modest lateral structure. This coupling is seen in section 4 to have a large signature in the time domain on some records, both data and synthetic.

In this study our primary interest is the effect of long-wavelength upper mantle structure on long-period surface wave observations. We restrict discussion to fundamental surface wave observations and neglect coupling to overtone modes ${}_nS_l$, ${}_nT_l$, where $n \neq 0$. The models of lateral structure used in the following experiments do not involve spherical harmonic expansions of order greater than 10. Angular selection rules for coupling between seismic modes severely restrict coupling between fundamentals and overtones for such models. The modes ${}_0S_l$ and ${}_nS_{l'}$ (or ${}_nT_{l'}$) will couple only in the presence of structure of angular order $s \geqslant l-l'$; $l-l' \gtrsim 10$ for most potential fundamental overtone coupling pairs in the frequencies of interest in this study. If one wished to calculate the low-frequency seismic response of a model with significant lateral structure of order $s > 10$, coupling to overtones may be important.

Unless otherwise noted, all synthetic seismograms are constructed to be 20 hours in length with a sampling time of 40 s. For comparison in the time domain with data records, a filter is applied to the synthetic records to minimize ringing in the time domain caused by the abrupt frequency cutoff at ${}_0S_{56}$. Data records are decimated to 40-s sampling interval and subjected to an identical filter. We choose for comparison only records from shallow events without appreciable overtone energy.

Although much of the waveform behavior reported in this section can be appreciated qualitatively, a proper evaluation of the effects of free oscillation coupling on waveform inversion schemes demands a quantitative analysis. The depth dependence of lateral structure is reflected in the frequency dependence of waveform anomalies. Therefore a quantitative assessment of waveform anomalies requires the application of spectral correlation techniques. We will compare the phase shift, amplitude, and apparent refraction of synthetic Rayleigh wave packet arrivals. Since the great circle transit time for long-period Rayleigh waves $\lesssim 3.2$ hours, one ordinarily cannot expect to isolate packets in time windows of length much greater than 1 hour. At 40-s sampling, one obtains 90 data points for a 1-hour time series. The Nyquist frequency of the discrete Fourier transform $(2\Delta t)^{-1} = 12.5$ mHz. The frequency content of the synthetic seismograms is limited to $f \lesssim 6.2$ mHz, so aliasing is not a problem. The nominal frequency spacing is $1/T \cong 0.028$ mHz. This can be reduced by padding the time series with zeroes. Zero padding by itself allows the resolution of some spectral features that lie between the frequency points

$$\{n/T\}_{n=0}^{T}$$

of the Fourier transform but cannot resolve spectral variation of scale length less than $1/T$.

Thomson [1982] has introduced a package of high-resolution spectral techniques that can, in many test cases, decrease the scale length of resolvable spectral variation via an adroit minimization of spectral leakage. One solves for "eigentapers" $w_k(t)$ $k=0,1\ldots,K-1$ by means of an optimization equation. In the following analysis we have used the first three 2π-prolate spheroidal sequences [*Slepian*, 1983] $w_k(t)$, $t=\Delta t, 2\Delta t, \ldots, (N-1)\Delta t, N\Delta t = T$, shown in Figure 1. These three tapers sample the data series in a statistically independent manner and have associated eigenvalues $\lambda_0 = 0.999948$, $\lambda_1 = 0.997765$, $\lambda_2 = 0.962155$ that correspond to the fraction of spectral energy at cycle frequency f_0 that is retained in the calcu-

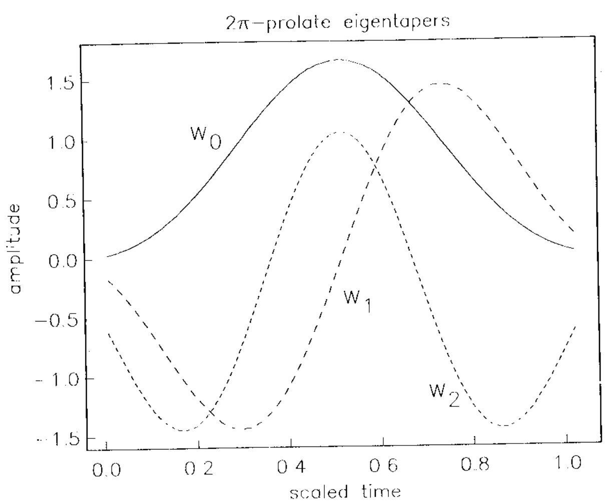

Fig. 1 Shapes of the three lowest-order 2π-prolate eigentapers $w_0(t)$, $w_1(t)$, $w_2(t)$; $w_0(t)$ is graphed with a solid line; $w_1(t)$ has one node and is graphed with a coarsely dashed line. $w_2(t)$ is graphed with an irregularly finely dashed line.

lated transform within the frequency interval $f_0 - 2/T < f < f_0 + 2/T$. $1-\lambda$ expresses the relative amount of spectral energy that leaks outside this interval. The utility of these data tapers is demonstrated in Figure 2, in which the Fourier transforms $W_k(f)$ of the first three 2π-prolate eigentapers are compared to that of the boxcar (untapered) window. These plots represent the convolution kernels for the transformed data series showing the amplitude transform of a single sinusoid. It is clear from the graph that the eigentapers trade a somewhat wider central lobe for greatly decreased side lobes, compared to the boxcar. The narrower central lobe of the boxcar is moot in a correlation analysis of two time series, as stability of the correlation coefficient will demand an averaging over adjacent frequency samples. The advantages of using multitapers for correlation analysis are discussed by Park, et al. (manuscript in preparation, 1985).

In *Thomson's* [1982] scheme, one Fourier-transforms the time series after application of each of the three eigentapers, obtaining three "eigenspectra." These eigenspectra are statistically independent estimates of the frequency content of the time series, under stochastic assumptions. One estimates the spectrum by averaging over squared eigenspectra at a given frequency. In this manner one obtains a local average while retaining excellent resistance to spectral leakage. Figure 2 indicates that the third 2π-prolate eigentaper has side lobes only slightly lower than those of the boxcar. In the noise-free synthetic comparisons reported in this section, this did not prove a significant handicap. Spectral estimation of noisy data series, however, would more safely be attempted with only the first two eigenspectra, neglecting the third as unreliable. An adaptive eigentaper algorithm that will accomplish this automatically is discussed by *Thomson* [1982] and Park et al. (manuscript in preparation, 1985).

Given two time series of seismic motion $u^{(0)}(t)$, $u^{(1)}(t)$, $t = \Delta t, \ldots, (N-1)\Delta t, N\Delta t = T$, with $u^{(0)}(t)$ taken as the "control" series for later error calculations, we calculate eigenspectra $y_k^{(j)}(f)$ for $k = 0, 1, 2$ and $j = 0, 1$:

$$y_k^{(j)}\left(\frac{n}{T'}\right) = \sum_{n'=1}^{N'} w_k(n'\Delta t)\, u^{(j)}(n'\Delta t)\, e^{inn'\Delta t/T'} \qquad (16)$$

where $N'\Delta t = T'$ and $N' > N$ is a power of two to enable a fast Fourier transform. $w_k(n'\Delta t) = u^{(j)}(n'\Delta t) = 0$ for $n' > N$. We wish to correlate $u^{(0)}$ and $u^{(1)}$ over a frequency band $(n_1/T') \leq f \leq (n_2/T')$. Form two vectors $\mathbf{y}^{(0)}$ and $\mathbf{y}^{(1)}$ so that

$$(\mathbf{y}^{(j)})_{3(n-n_1)+k} = y_k^{(j)}\left(\frac{n}{T'}\right) \qquad (17)$$

and minimize $\mathbf{y}^{(0)} - c\mathbf{y}^{(1)}$ in a least squares sense to find the complex correlation coefficient c. It is easy to show that

$$c = \frac{(\mathbf{y}^{(0)})^{*}\cdot\mathbf{y}^{(1)}}{|\mathbf{y}^{(0)}|^2}$$

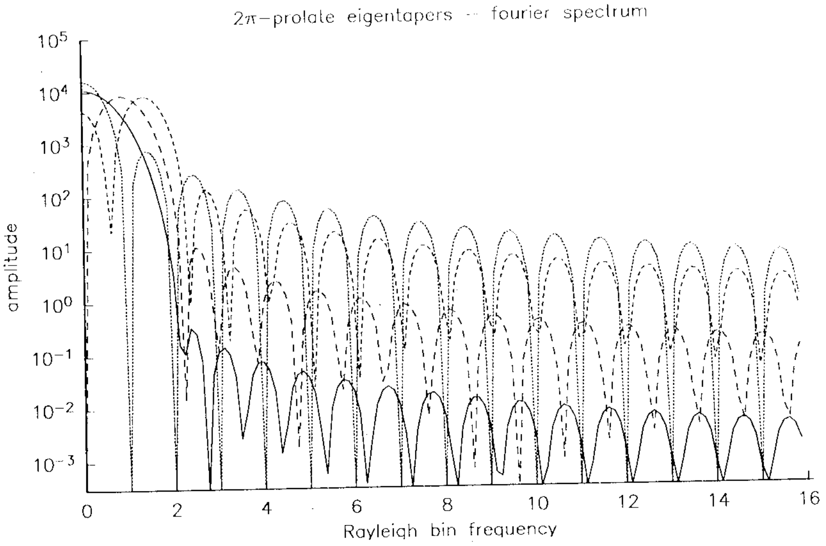

Fig. 2. Fourier amplitude transforms of the 2π-prolate eigentapers $w_0(t)$, $w_1(t)$, $w_2(t)$, using line weights identical to those used in Figure 1. The Fourier amplitude transform of the boxcar window is plotted for comparison with a dotted line. Note that although the boxcar transform has a central lobe with half the width of the central lobes of the 2π-prolate transforms, all of the latter transforms possess significantly lower side lobes beyond the central lobe.

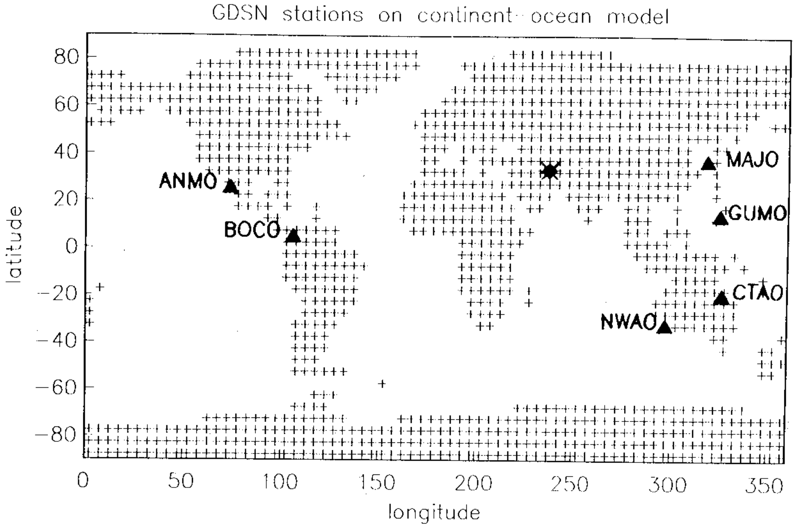

Fig. 3. Continent-ocean pattern derived from GTR1 model of *Jordan* [1981]. Epicenter of 1978 Tabas, Iran, event is indicated, along with the positions of the six GDSN stations used in off-path sensitivity experiment.

$|c|$ is interpreted as the amplitude ratio of the two series at cycle frequency $f_c = (n_1+n_2)/(2T')$. $\mathrm{Arg}(c)(2\pi f_c)^{-1}$ is the phase shift in units of time. If the control series has both north and east horizontal components and an apparent back azimuth $\theta^{(0)}$ at the receiver, $\tan\theta^{(1)} = |c_E|/|c_N| \tan\theta^{(0)}$, where the subscripts E, N refer to east and north, respectively, as long as the perturbation does not change quadrants in the unit circle (and thus change the sign of the tangent).

The uncertainty in c can be estimated from the fractional least squares misfit $\epsilon^2 = \|\mathbf{y}^{(0)} - c\mathbf{y}^{(1)}\|^2/\|\mathbf{y}^{(0)}\|^2$. The noise variance estimate $\sigma^2 = \epsilon^2/(M-2)$, where M is the degrees of freedom present in the least squares regression. We subtract two to account for the two degrees of freedom present in the complex correlation coefficient c. We have fewer degrees of freedom than twice the number of complex-valued spectral estimates in the regression, as we have padded with zeroes to a power of two. This suggests multiplication by N/N', the ratio of the unpadded to the padded length. No fewer than $2 \times 3 = 6$ degrees of freedom are represented, since the three windowed transforms are statistically independent. There is an upper limit as well, since the spectral leakage resistance of the 2π-prolate tapers limits the spectral information gathered to the bandwidth $(n_1/T') - (2/T) \leqslant (n_2/T') + (2/T)$. Therefore our regression can have no more than $2((n_2-n_1)T/T'+4)$ degrees of freedom. We have estimated M from the following formula.

$$M = \max\,(6, M') \tag{18}$$

where

$$M' = \min\,\{6(n_2-n_1+1)\;T/T',\;\; 2[(n_2-n_1)\;T/T'+4]\}$$

M and M' need not be integers for the purpose of scaling σ^2. Once σ^2 is estimated from the regression misfit, it is straightforward to calculate the resultant uncertainty in correlation amplitude, phase shift, and apparent refraction angle.

2. SIMPLE OBSERVABLES AND OFF-PATH SENSITIVITY

We illustrate the behavior of coupled-mode synthetics with examples drawn from a synthetic experiment. Figure 3 shows the Mercator projection of the continents and oceans, based on the GTR1 regionalization of *Jordan* [1981] with trenches taken to be continental. The epicenter of the 1978 Tabas, Iran, event and six GDSN stations are indicated. The stations were chosen so that the epicentral distance Δ lies between 60° and 120°, enabling the isolation of Rayleigh packet arrivals in time windows of one-hour length. We used the moment tensor solution

TABLE 1. Components of Moment Tensors

				Moment, 10^{27} dyne cm						
Position	Year	Day	Depth, km	m_1	m_2	m_3	m_4	m_5	m_6	Region
22.88°S, 175.9°W	1977	173	65	−7.05	0.47	6.58	3.16	11.80	1.76	Tonga
8.03°S, 155.54°E	1977	210	33	0.09	−0.09	0.00	0.10	0.27	0.69	New Ireland
11.09°S, 118.46°E	1977	231	20	−26.48	23.57	2.91	0.20	−0.62	8.31	Sumbawa
33.39°N, 57.43°E	1978	259	7	1.02	−0.46	−0.56	0.01	0.01	0.51	Tabas
16.01°N, 96.59°W	1978	333	18	1.33	−1.29	−0.04	1.8	−0.32	0.23	Oaxaca
46.06°N, 151.45°E	1980	366	33	−2.00	1.00	1.00	0.00	0.00	1.00	Kurile

All source mechanisms except the last are due to an as yet unpublished study by G. Masters et al. The Kurile mechanism is that of a thrust double-couple with 45° strike, 45° dip.

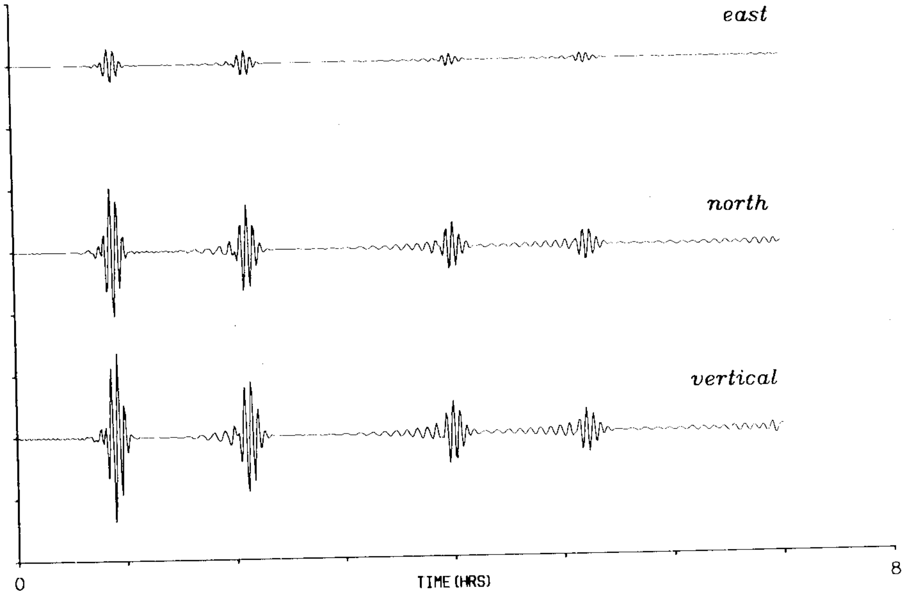

Fig. 4. Synthetic seismogram for ANMO calculated using spheroidal modes ${}_0S_l$, $2 \leqslant l \leqslant 56$, with coupling between neighboring multiplets calculated for model M84A of *Woodhouse and Dziewonski* [1984]. The first 7 hours of synthetic data are shown. A residual bandage effect can be seen in the vertical component synthetic prior to the first Rayleigh wave arrival R_1.

given in Table 1. The source is predominantly dip-slip, with 139.4° strike (measured clockwise from north) and 45.0° dip. The radiation pattern for 256-s surface waves is shown by *Lay and Kanamori* [1985] to vary by a factor of 3 from maximum to minimum with constant phase and no nodal points. Hybrid spheroidal singlets were calculated for the continent-ocean model of Figure 3, with a surficial spherical harmonic expansion up to angular order and degree 10. A 2.3% difference in shear velocity between continents and ocean was imposed, a value consistent with the *ScS* studies of *Sipkin and Jordan* [1976, 1980], when extrapolated to free oscillation frequencies. We obtain perturbations in κ, μ, ρ by using the scaling relations

$$\frac{\delta\rho}{\rho} = 0.4\,\frac{\delta\beta}{\beta} \qquad \frac{\delta\alpha}{\alpha} = 0.8\,\frac{\delta\beta}{\beta} \tag{19}$$

suggested by the thermal behavior of mantle rocks and used to stabilize inversion procedures in several recent seismic studies of upper mantle structure [*Masters et al.*, 1982; *Woodhouse and Dziewonski*, 1984]. The anomaly was assumed to extend from the Moho to 420 km depth in model 1066A. The effects of hydrostatic ellipticity and rotational splitting were also included. We used the coupling recipe that considers nearest-neighbor multiplets ${}_0S_{l-1} - {}_0S_l - {}_0S_{l+1}$, sensitive to both even and odd lateral structure. Synthetic seismograms containing only fundamental Rayleigh waves were computed for this recipe and for a control calculation which included rotational and elliptical splitting. Any difference between the two sets of seismograms is attributable to the continent-ocean structure.

The first 7 hours of coupled-mode synthetic data appropriate to station ANMO are shown in Figure 4. The first four Rayleigh wave packets R_1, R_2, R_3, R_4 are evident on all three components, with a noticeable increase in dispersion with orbit number. Since toroidal modes are excluded, there are no Love waves. The effect of lateral structure is evident in the overlay of coupled-mode synthetic (dashed line) and spherical earth synthetic (solid line) shown in Figure 5. Although the waveforms are quite similar, the coupled-mode R_3 is distinctly early. A small phase shift can be discerned in R_4 as well. The short orbit on the great circle connecting Tabas and ANMO contains roughly 80% continent in the $s \leqslant 10$ spherical harmonic expansion of the continent-ocean function. Since the average value expected for the model in Figure 3 is 38.9% continental and continents are taken to be faster, it is not surprising that R_3 is noticeably early. The long orbit represented by R_4 traverses much more ocean, averaging 38.1% continent in the roughly 1.7 earth transits from earthquake to R_4 arrival.

Spectral correlation between control and coupled-mode synthetics produces graphs of time delay, translatable into a surface wave phase velocity anomaly as a function of frequency. In Figure 6 are shown the results for R_1 through R_4 on the ANMO vertical record. (The horizontal comparisons in this case do not differ significantly.) Odd-order Rayleigh packets R_1 and R_3, whose orbits traverse more continent than the average, have early arrivals compared to the even-order packets R_2 and R_4. The great circle travel times $R_3 - R_1$ and $R_4 - R_2$ appear roughly equivalent. The tomographic prediction for time delay as a function of frequency can be obtained by calculating degenerate frequency shifts for earth models with entirely "continental" or "oceanic" upper mantle structure. A path-dependent frequency shift (and hence a surface wave phase shift) are obtained from a linear combination of the "continental" and "oceanic" frequency shifts corresponding to the fraction of the great circle source-receiver paths spent in each of the two regions. Since the continent ocean model is expanded in spherical harmonics of degree $s \leqslant 10$, calculating the path fraction is accomplished via line integrals of spherical harmonics. Figure 7

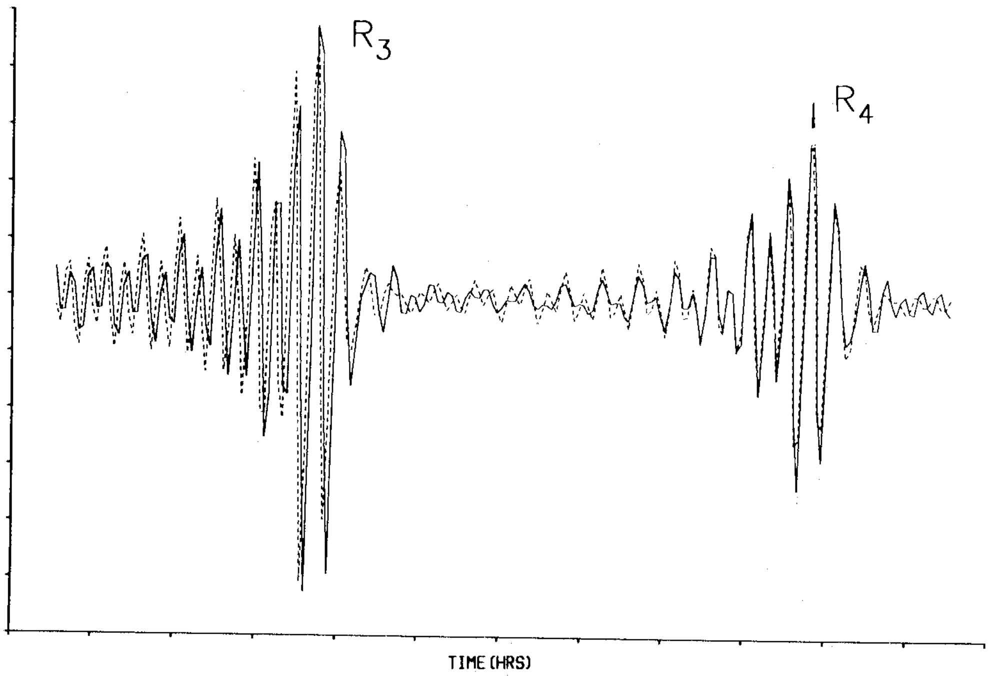

Fig. 5. Comparison of ANMO vertical component synthetics. Dispersion branch coupled synthetic (dashed line) is plotted over the uncoupled spherical earth synthetic (solid line).

compares predicted versus observed time delays for R_1 and R_2 on the ANMO record. The agreement is not exact but is reasonable.

Stronger off-path sensitivity is evident in some of the measured great circle phase delays. Figures 8 and 9 show phase delay times of $R_{n+2}-R_n$, $n=1,2,3$ for GDSN stations BOCO and NWAO, respectively. The geometric ray phase delay prediction is indicated by a solid line in Figures 8 and 9. The measured BOCO delays show a trend where none is predicted. Moreover, the several $R_{n+2}-R_n$ measurements have values that differ significantly relative to the 1σ error bars. This indicates that the successive "great circle" orbits do not sample the same structure. The discrepancies (Figure 9) evident in phase delays for the NWAO waveforms are larger than those of BOCO, but the great circle path prediction at least shows the correct trend. Here the discrepancies between distinct great circle orbit delays increase with increasing frequency (decreasing period), becoming significant above 4.5 mHz. However, the significant size of apparent off-path bias effects relative to the typical phase shift signal of 10–40 s found in global studies suggests an unwelcome limit to our ability to resolve earth structure using great circle surface wave dispersion.

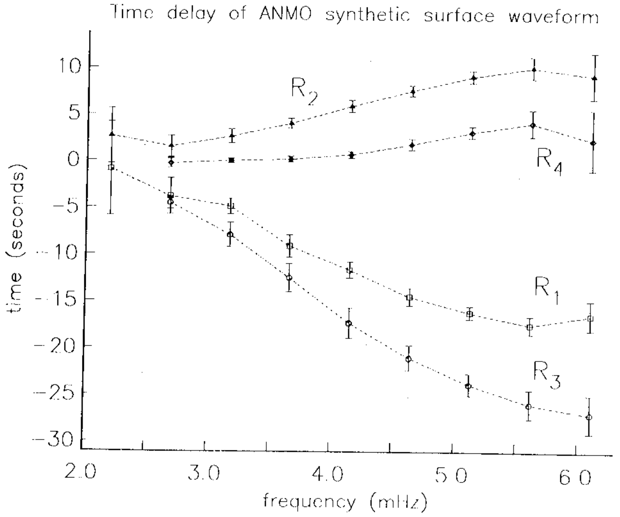

Fig. 6. Waveform time delay as a function of frequency for R_n, $n=1,2,3,4$, on the ANMO vertical component coupled-mode seismogram, relative to the spherical earth control synthetic. Individual time delay estimates are plotted with error bars and connected by dashed lines to facilitate differences between Rayleigh wave packets.

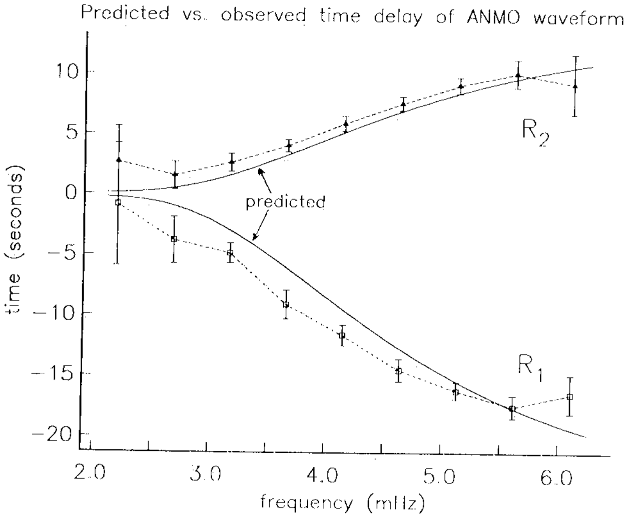

Fig. 7. Waveform time delay comparison between the delay measured for R_1 and R_2 on ANMO vertical component and the great circle (tomographic) predicted time delay. The measured delay values are plotted with error bars and connected with dashed lines. The predicted time delay is graphed with smooth solid curves.

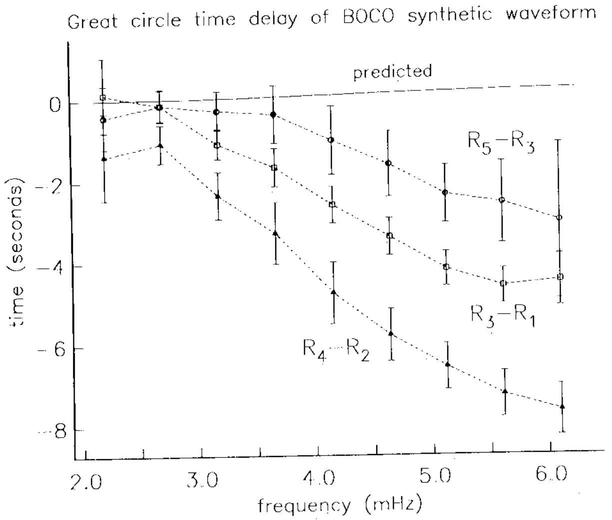

Fig. 8. Waveform time delay comparison for the BOCO vertical component synthetic. The great circle time delay measured relative to the spherical earth synthetic for wave packet pairs $R_{n+2}-R_n$, $n=1,2,3$ using the 420-km-deep continent-ocean model are plotted as a function of frequency and connected with dashed lines. The tomographic great circle delay prediction is graphed with a solid curve. The measured discrepancies imply off-path sensitivity for the Rayleigh waves.

Lay and Kanamori [1985] and *Wong and Woodhouse* [1983] have traced geometric rays through recent models of lateral structure in the upper mantle. They find that these rays wander significantly off the great circle paths, often arriving at the receiver at a deflected azimuth. Similar behavior can be inferred from the horizontal BOCO and NWAO synthetics. The apparent refractions of these waveforms are graphed versus Rayleigh orbit number in Figures 10 and 11. The azimuth of the great circle path is indicated by the solid line. Results are shown at $f = 3.2$ mHz and $f = 5.6$ mHz. The BOCO graphs in Figure 10 show clearly a divergence of azimuth between even and odd Rayleigh orbits. The 3.2-mHz waveform component is less sensitive to upper mantle structure than the 5.6-mHz energy, and so is refracted less. The NWAO values graphed in Figure 11 show a one-sided refraction, with only odd orbits significantly distinct from the great circle azimuth. Perusal of Figure 3 suggests that the odd orbit wave packets are refracted by the high-velocity continental region of South Asia.

NWAO and BOCO lie 20° and 6°, respectively, away from minima in the radiation pattern of the modeled source. If this minimum were a node in the pattern, one might not be surprised to see off-path propagation effects in the synthetic seismograms. The derivative of the Tabas radiation pattern vanishes at its minima, so that seismic energy radiating at nearby values of source azimuth is not appreciably larger in amplitude. The off-path propagation effects discussed above are not an artifact of the radiation pattern. If the strike of the dip-slip source model used is rotated 90° so that NWAO and BOCO lie near the maxima

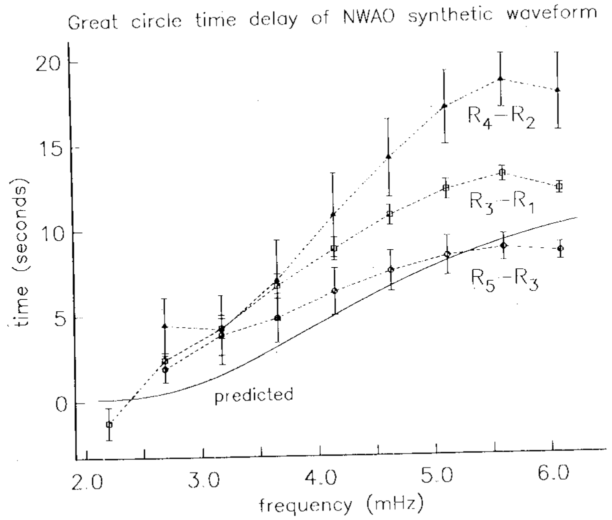

Fig. 9. Waveform time delay comparison for the NWAO vertical component synthetic. The great circle time delay relative to a spherically averaged earth is plotted with error bars for $R_{n+2}-R_n$, $n=1,2,3$ and connected with dashed lines. The tomographic great circle prediction is graphed with a solid curve.

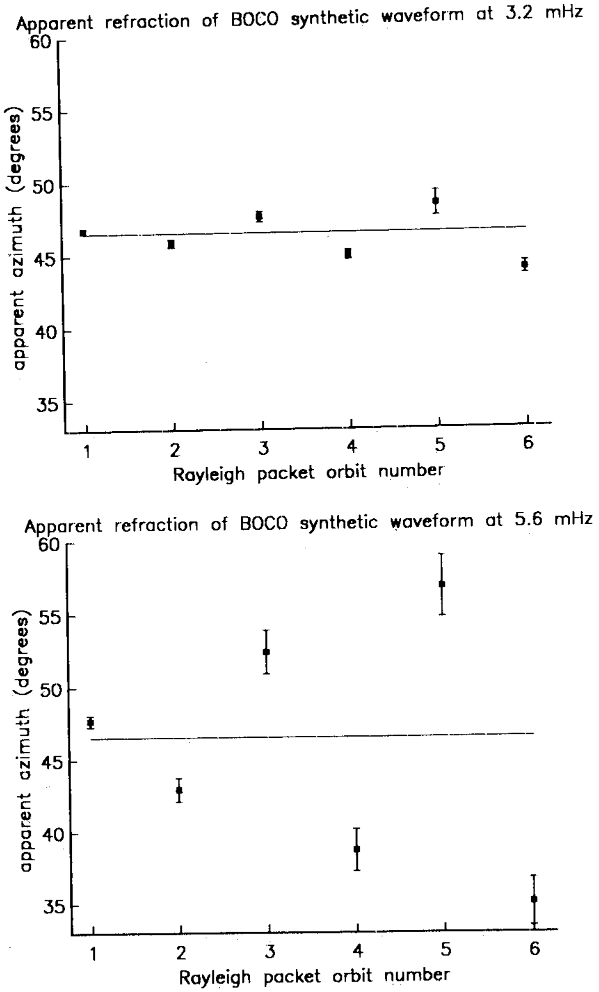

Fig. 10. Apparent refraction of BOCO synthetic Rayleigh wave packets R_n, $n=1,\ldots,6$. Apparent azimuth is found from the ratio of NS and EW horizontal components, measured for each wave packet at chosen frequencies. Receiver azimuth values in degrees are plotted with error bars versus wave packet number. The great circle azimuth is indicated with the solid line. Azimuth measurements are given for $f = 3.2$ mHz and $f = 5.6$ mHz. Note how the azimuth perturbation alternates with order number. Overall deflection increases at the higher frequencies.

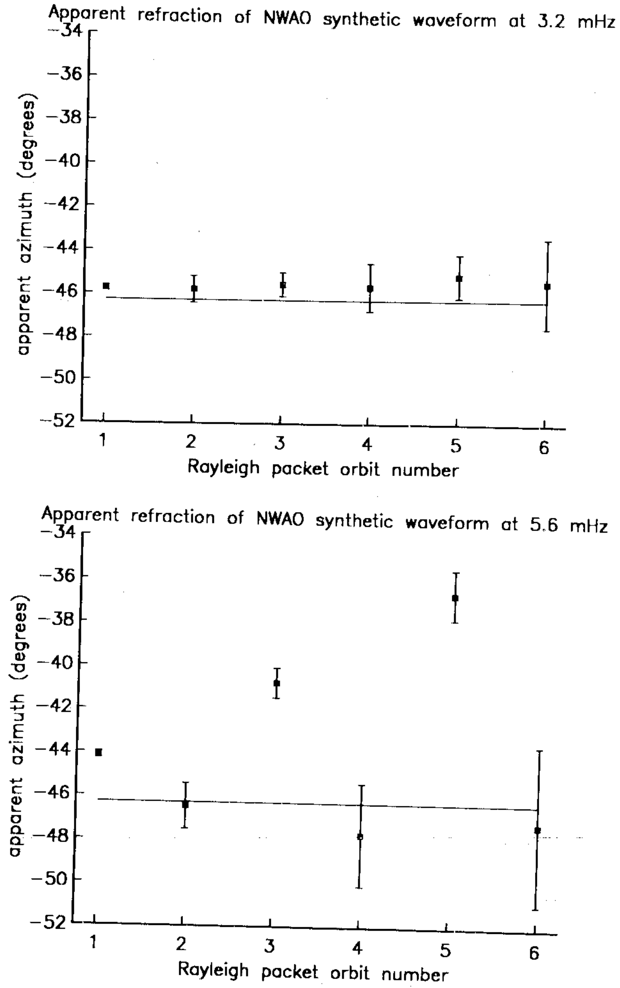
Apparent refraction of NWAO synthetic waveform at 3.2 mHz

Apparent refraction of NWAO synthetic waveform at 5.6 mHz

Fig. 11. Apparent refraction of NWAO synthetic Rayleigh wave packets R_n, $n = 1,\ldots,6$. Note that the even wave packets are not significantly deflected.

in radiation amplitude, the same refraction effects are observed.

In these examples, deflections as great as 10° are measured for R_5 and R_6. Apparent deflections as great as 20° have been observed in GDSN records [*Masters et al.*, 1983*b*]. Such deflections are plausible if, as suggested by the models of *Woodhouse and Dziewonski* [1984] and *Nakanishi and Anderson* [1984], lateral variations $\geq 8\%$ exist in the uppermost mantle. Moreover, the simple dependence of these examples with Rayleigh orbit number encourages the application of surface ray-tracing schemes, in which deflection also tends to increase with orbit number.

3. TRAVELING WAVE EFFECTS: AMPLITUDE ANOMALIES AND PHASE SHIFTS

The effects of lateral structure on traveling surface waves can be studied with coupled-mode seismograms. The prominent observable quantities are the anomalies in measured amplitude of surface wave packets and the phase shift caused by perturbations in phase velocity. The latter effect is well-known to seismologists and has been the focus of many inversion schemes. Amplitude anomalies are often ignored, since they are both harder to model and because their study requires a more thorough knowledge of the instrument calibrations than is often routinely obtainable. *Niazi and Kanamori* [1981], however, showed IDA data from a September 16, 1978, event in Tabas, Iran ($M_S = 7.4$), that contained dramatic variations in surface wave amplitude that were unambiguously related to lateral structure. Five IDA records for this event, low-passed to include energy with $f \leqslant 6.2$ mHz, are shown in Figure 12. R_1 saturated the instruments and was discarded. The traces are ordered by the azimuth at the epicenter of the source-receiver great circle. On an earth whose properties vary only with radius, successive Rayleigh wave arrivals decay monotonically in amplitude. This behavior is not followed by the Tabas data. The trace from CMO (College, Alaska) shows the amplitude of R_2 smaller than that of R_3, and R_4 much smaller than R_5. R_6 appears to have vanished. The alternating pattern of Rayleigh packet amplitudes is reverse in the PFO (Piñon Flat, California) and KIP (Kipapha, Hawaii) records, which closely bracket CMO in source azimuth. This reversal of pattern within the azimuth of a single lobe of the radiation pattern rules out source directivity as a contributing factor. Multipathing effects are implausible at these low frequencies, since the phase shift required to enable destructive interference would require unreasonably large lateral velocity variations. The lateral ray-tracing reported by *Lay and Kanamori* [1985] and *Wong and Woodhouse* [1983] suggest focusing and defocusing of surface wave energy as the major factor in these anomalies. The full wave propagation description afforded by coupled-mode seismograms will serve as a check on ray-tracing results and perhaps suggest alternative descriptive approximations.

Coupled-mode IDA synthetic seismograms using fundamental spheroidal free oscillations and model M84A produce many examples of anomalous wave packet ampli-

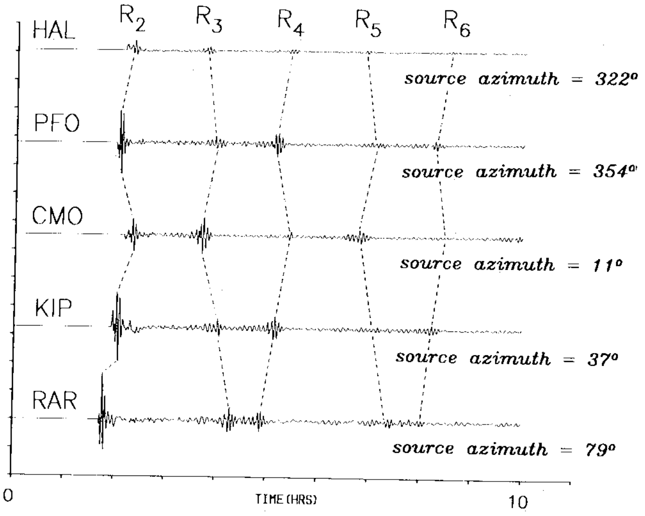

Fig. 12. IDA data from 1978 Tabas, Iran, event. The first 10 hours after the event are shown. R_1 for this event caused the instruments to go nonlinear and was omitted.

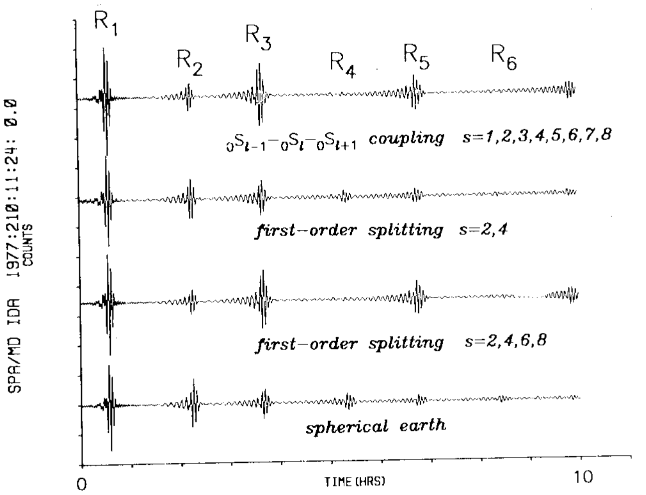

Fig. 13. Synthetic IDA records from an event in the New Ireland region (8.03°S, 155.54°E) using an assortment of coupling recipes. First 10 hours are shown.

tudes. One case is shown in Figure 13, for a SPA (south pole) record of a synthetic seismic source in the New Ireland region. The spherical earth seismogram is plotted at the bottom as a control. A first-order splitting calculation, sensitive to even-angular orders in M84A, is juxtaposed above the control. R_2, R_4, and R_6 are deficient in amplitude, the latter two having disappeared altogether. R_3, R_5, and a hint of R_7 are clearly enhanced. Another first-order splitting calculation is shown in which M84A was truncated at $s = 4$. The anomalous amplitudes persist but are much less evident. The top trace shows the results of a dispersion branch coupling calculation, sensitive to both even- and odd-order lateral structure. This trace does not differ visually from the first-order splitting calculation using an untruncated M84A.

Spectral analysis of the individual wave packets, isolated in 1-hour time windows, affords a glimpse of the frequency dependence of the amplitude anomalies. Spectral amplitude ratio results for R_n, $n = 1, \ldots, 5$ are shown in Figure 14. Amplitude variation is relatively small for $f < 3$ mHz, rises between 3 and 4 mHz, and levels off or varies slowly above 4 mHz. The behavior agrees with the hypothesis that amplitude anomalies can be explained in terms of the divergence of lateral rays, as the ray approximation improves with increasing frequency. The amplitude ratio for R_4 has a minimum of $f \approx 4$ mHz, which may indicate depth-dependent refraction. Another notable feature is the apparent reversal of the sense of anomaly for R_4 and R_5 at $f \approx 2.5$ mHz. This is not caused by depth-dependent refraction but rather by the dispersion of surface wave group velocity at low frequencies. The time window that encloses the visible wave packet R_4 does not contain the energy of R_4 at periods $T \gtrsim 400$ s. The nominally larger amplitudes at those frequencies belong to the low-frequency component of R_5, traveling with a substantially higher group velocity than that of the main wave packet. In a like manner, the nominally deficient long period components of R_5 are the dispersed precursors to the main wave packet of R_6.

Although differences between the first-order splitting and dispersion branch coupling traces are difficult to detect visually, they can be seen in a numerical analysis. A plot, similar to Figure 14, comparing spectral ratios of $R_1 \cdots R_4$ between the two coupling schemes is given in Figure 15. Aside from R_4, where the dispersion branch coupled seismogram does not exhibit the amplitude ratio minimum seen in Figure 14, the spectral amplitudes vary by no more than 13% with smooth variation in frequency. The measured time shifts between the two coupling schemes for R_1, R_2, R_3 are shown in Figure 16. R_4 was not included as its low amplitude led to high uncertainties. $|\Delta t| < 4$ s in all measurements shown, much smaller than

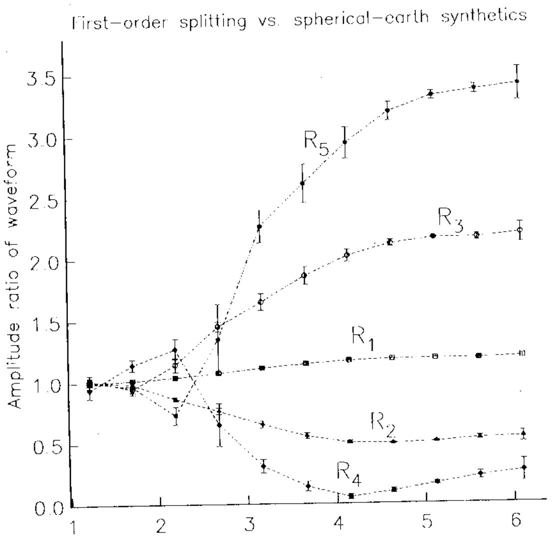

Fig. 14. Amplitude ratio as a function of frequency for first-order splitting synthetic Rayleigh wave packets R_n, $n = 1, \ldots, 5$, relative to spherical earth wave packet amplitudes. Measured ratios are plotted with error bars and connected with dashed lines to distinguish distinct wave packets. Ratios are measured for SPA records shown in Figure 13.

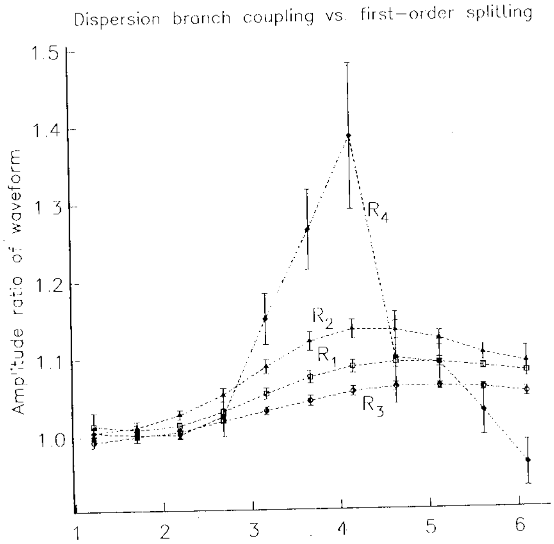

Fig. 15. Same as Figure 14 but with comparison between the same-branch coupled-mode synthetic and the first-order splitting synthetic.

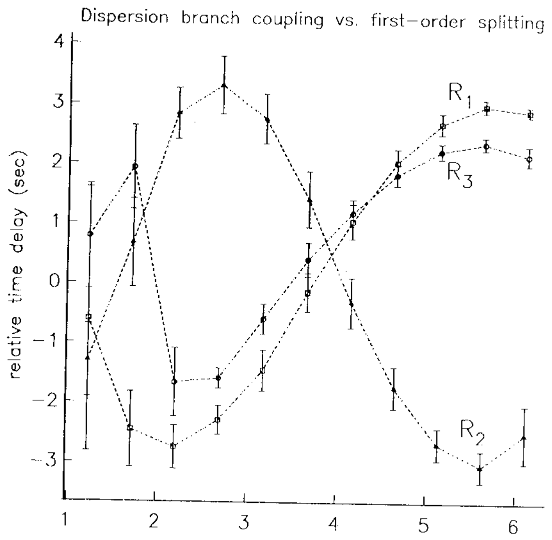

Fig. 16. Time delay for dispersion branch coupled synthetic relative to first-order splitting in the SPA synthetics of Figure 13. Values for R_n, $n = 1, 2, 3$, are graphed versus frequency.

the time shifts measured between either of the coupling schemes and the spherical earth seismogram. The small 1σ error bars in Figure 16 indicate how closely matched the two coupled-mode waveforms are. The absolute uncertainty in time shift is much greater when the coupled-mode and spherical earth waveforms are correlated.

Variation in source mechanism affects the relative amplitude anomalies of synthetic records in some cases. The example used in Figure 13 is generated using the source mechanism given in Table 1. The moment tensor corresponds to a predominantly strike slip event with focal planes at strike = 1.4°, dip = 83.4°W and strike = 94°, dip = 68.6°S. The great circle connecting source receiver SPA intersects the focal sphere at due north and south, quite close to the radiation nodes for Rayleigh waves. The large anomalies seen are consistent with the intuition that unusual propagation effects are more commonplace near radiation nodes. We performed a small experiment in which we fabricated a set of sources at the New Ireland hypocenter, each pure strike slip with values of strike = −45°, −30°, −15°, 0°, 15°, 30°, 45°. The dramatic amplitude anomalies seen in Figure 13 were evident for the 0° strike test only, but visible amplitude anomalies were present in all but the −45° strike example. Anomalously small amplitudes (e.g., 30% deficient) were most often noted for R_4, but the 15° strike example possessed amplitude deficiencies in R_3 and R_5 rather than the even-order wave packets.

Another example is given in Figures 17 and 18, showing spherical earth and first-order splitting synthetics, respectively. A strike-slip source at the hypocenter of the 1977 Sumbawa event was used. Three sources are compared, with strike angles 35°, 45°, and 55°. IDA station SSB lies quite close to the Rayleigh radiation node at 45° fault strike. This is evident in the spherical earth synthetics of Figure 17 in which the relative amplitude of the 45° source-strike trace nearly vanishes. The bracketing traces are mirror images of each other, representing the compressional and dilatational lobes of the radiation pattern. The coupled synthetics of Figure 18 exhibit amplitude anomalies. The 45° source-strike trace amplitude is boosted by wave energy that travels off-path. The bracketing traces show clear alternate packet amplitude anomalies but in opposite senses. The 35° source-strike trace has small-amplitude even orbits and large-amplitude odd orbits. The 55° source-strike trace shows the opposite pattern. Since the source mechanism in all cases is a point-source double-couple, no directivity effects can be involved. The periods of these wave packets are too long to be susceptible to multipathing interference. The explanation must come from off-path propagation between source and receiver.

In section 2 we saw apparent wave packet ray path deflection of 10°−20° at the receiver. The situation is no different when wave packet energy is projected back to the source. In general, the seismic energy seen in an individual surface wave packet emanates from a finite beamwidth about the source-receiver great circle azimuth (Figure 19). The amplitude of an arriving wave packet will depend on how the energy across the beam is focused by the intervening lateral structure, and on the relative weighting across the beam of the source radiation pattern. If the source radiation pattern varies strongly across the width of the beam, a perturbation in the source parameters can significantly alter the relative weighting of the beam components. Such an effect is more prevalent near nodes of the radiation pattern, where absolute amplitudes are lower and both compressional and dilatational radiation lobes can contribute energy. At or near lobe antinodes, the source radiation varies little across the beam. The result is illustrated for first-order splitting in Figure 20. A thrust source in the Kurile trench is modeled at IDA station SUR. Although a variation in absolute amplitude occurs as the source strike varies by 40°, the relative $R_3 - R_4$ amplitude anomaly remains unchanged.

We tested dispersion branch coupled synthetics made with model M84A against some visibly anomalous IDA records. The results for the Tabas event of 1978 using the source mechanism of *Masters et al.* [1983*b*] were not encouraging (Figure 21). The only visible anomaly is the amplitude deficiency of R_4 on the CMO record relative to R_3 and R_5. None of the other large-amplitude variations in the data (Figure 12) are found. We varied the source mechanism about the chosen source mechanism but observed little variation.

IDA records from events in the New Hebrides region show visible wave packet amplitude anomalies. The source-receiver propagation paths for these events are much different than those from Iran and therefore provide an independent test of M84A. We used a July 15, 1981 event at 17.34°S, 167.27°E with a shallow reverse-fault mechanism. We use the source parameters found by *Dziewonski and Woodhouse* [1983], who gave a moment tensor $\mathbf{m} = (4.78, -0.65, -4.14, 0.04, -3.3, 1.31)$ in units of 10^{26} dyne cm, with source depth 30 km. The source is predominantly dip-slip, with focal planes defined by 161.2° strike, 32.0°NE dip, and 171.6° strike, 58.4°SW dip. As with the Tabas source mechanism, the radiation pattern does not have nodes, but rather amplitude minima about which the excitation amplitude is slowly varying and the

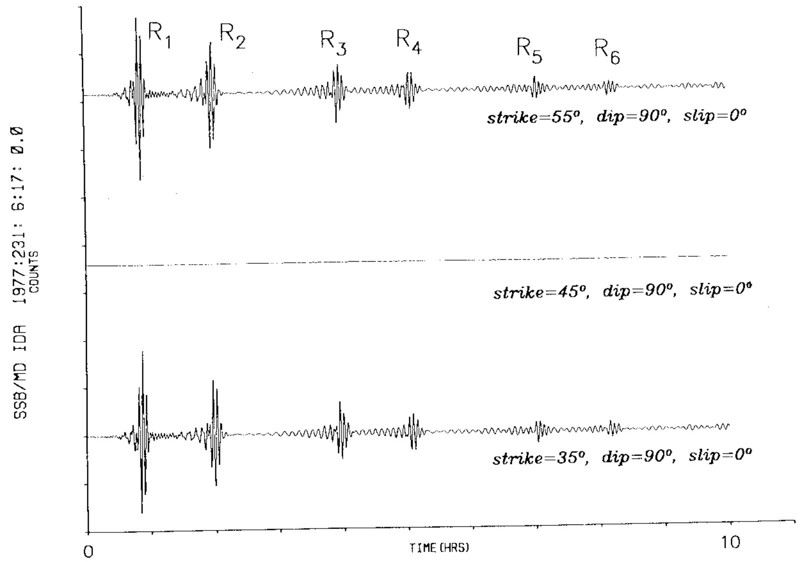

Fig. 17. Spherical earth (uncoupled) synthetics for IDA station SSB for a source at the hypocenter of the 1977 Sumbawa event. Synthetic records appropriate to three strike-slip sources are shown. The central trace has the Rayleigh wave radiation node aligned with the source-receiver great circle.

phase is constant. All New Hebrides events of 1981 reported by *Dziewonski and Woodhouse* [1983] had similar wave packet amplitude anomalies. The clearest examples, unobstructed by overtones and not obscured by low signal-to-noise, were in data from this event. After a low-pass filter removed signals with $f \gtrsim 6.3$ mHz, 8 of 12 usable IDA records possessed visible amplitude anomalies. Of these eight, model M84A predicted three, including the GUA record shown in Figure 22, where the data trace is compared with spherical earth and branch-coupled synthetics. Note that although the total amplitude of the trace is underpredicted by the source mechanism and structure, the relative amplitude anomaly between R_2, R_3, and R_4, R_5 is modeled quite well. Figure 23 shows a similar comparison for station BDF, in which M84A was unsuccessful in modeling an observed anomaly, i.e., the amplitude reversal of R_3 and R_4. The great circles for BDF and GUA from the epicenter vary by 11.5° at most, so that seismic surface waves measured at the two stations sample identical or nearby structures. At IDA station ESK, M84A synthetics predicted an anomaly that was not present in the data (Figure 24).

This lack of correspondence is not surprising in light of the full waveform inversion scheme used to construct M84A. A 20% amplitude anomaly, alternating excessive/deficient with odd/even orbit number, is visible in a seismic record. The difference seismogram, however, has relative amplitude 0.2 and therefore represents only a 4% misfit variance. An equivalent 4% variance misfit is caused by a 11.5° phase delay in the waveform. This

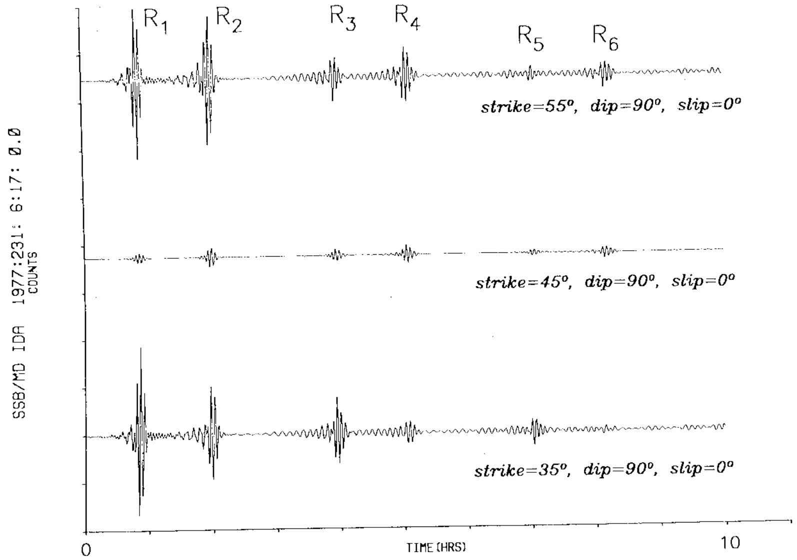

Fig. 18. First-order splitting synthetics for the source-receiver orientations of Figure 17. The central trace shows evidence of off-path scattering. The R_3-R_4 wave packet amplitude anomaly seen in the top and bottom traces have opposite sense.

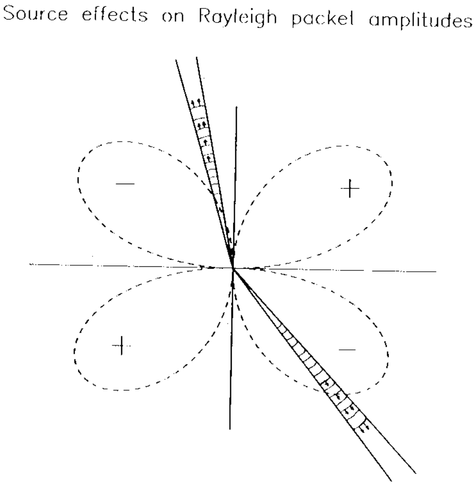

Fig. 19. Schematic of seismic source. The surface wave packet is assumed to represent energy that is contributed from finite beamwidths about the source-receiver great circle.

corresponds to only a 6.4-s time delay in a 200-s surface wave. The phase delay is less visible, but figures just as strongly in any attempt to minimize waveform misfit. The phase delays of both data and coupled-mode synthetics are typically much larger than 11.5°. In light of this, it may be necessary to account for amplitude anomalies separately from phase shifts in waveform inversion schemes if they can be shown to be robust indicators of lateral structure. It is possible that amplitude anomalies are complicated functionals of lateral structure in which shorter-wavelength ($s \gtrsim 20$) structure plays an important role. This is not unreasonable if the focusing and other refractive behavior of surface wave free oscillations with $l \sim 30-60$ is the cause of the observed anomalies. Therefore amplitude anomalies may not be useful constraints in inversion schemes for only long-wavelength ($s \lesssim 10$) lateral structure.

Given the capability to construct coupled-mode seismograms that are sensitive to either only even-order structure or even- and odd-order structure, it is useful to assess the effect of odd-order structure on the coupled-mode seismogram. One wishes to predict the amount of data variance that ought to be explained by a plausible amount of odd lateral structure. To this end we have performed an experiment with synthetic records from 132 source-receiver pairs. The events and source mechanisms used are given in Table 1. The location and instrument response of 22 past and present IDA station sites were used for each event — the current network contains 18 stations. We compared dispersion branch coupled synthetics and first-order splitting synthetics for all source-receiver pairs with teleseismic distance $55° \leqslant \Delta \leqslant 125°$, so as to avoid overlapping Rayleigh wave packets. Seventy-six out of 132 source-receiver pairs (58%) meet this criterion. For an even distribution of source-receiver positions this Δ constraint would retain 57% of the traces.

Although these traces are too few to obtain a reliable inversion for lateral structure, some observations can be made on the average waveform perturbations caused by lateral structure. Figure 25 shows the rms value of measured time delay caused by even-order structure in a first-order splitting calculation, relative to spherical earth synthetics. Values from R_1 to R_6 are plotted. The solid line graphs $|\Delta t|_{\mathrm{rms}}$ as a function of frequency. The solid circles connected by the dotted line graph the maximum out of 76 measured absolute time shifts. Note the tendency for $|\Delta t|_{\mathrm{rms}}$ to grow with increasing propagation distance to a value for R_6 of 40–50 s. Smaller time delays are noted at $f \lesssim 3.5$ mHz, not surprising since the perturbation of M84A is larger at shallower depths. The time delays that can be attributed to odd-order structure are graphed in Figure 26 where synthetics from first-order splitting and dispersion branch coupling are compared. The time shifts are much smaller, averaging ~5 s for all R_1–R_6. Individual record pairs, as the dotted lines show, can exhibit time delays of 15–25 s. The independence of $|\Delta t|_{\mathrm{rms}}$ with wave packet orbit number is expected, as the minor arc average $\delta\bar{\omega}$ formulated by *Woodhouse and Dziewonski* [1984] for odd-structure inversion is found by subtracting the travel times of neighboring wave packets. Under the assumption that the seismic wave packet does not stray from its great circle trajectory, $\delta\bar{\omega}$ is constant with increasing propagation distance. Figures 25 and 26 suggest that surface wave phase delays must be measured to a large relative precision if one hopes to detect odd-order structure with them. On this point it is discouraging to note the variability among great circle travel times R_3–R_1, R_4–R_2, and R_5–R_3. For synthetics that are sensitive only to even-order structure, the rms average variation among these orbit times varied between 3 and 5 s for $3.5 \lesssim f \lesssim 6.0$ mHz. This variation, as noted in section 2, is a departure from the great circle propagation assumption. It is also comparable in size to the time delays induced by the odd-order part of M84A.

Measurements of anomalous wave packet amplitude may also be used in future inversions. A similar generalization can be made about the relative perturbations of even- and odd-order lateral structure. Figures 27 and 28 show aggregate results of amplitude ratio measurements of R_1 through R_6 for 76 synthetic seismogram pairs used in the previous comparison. The individual measurements

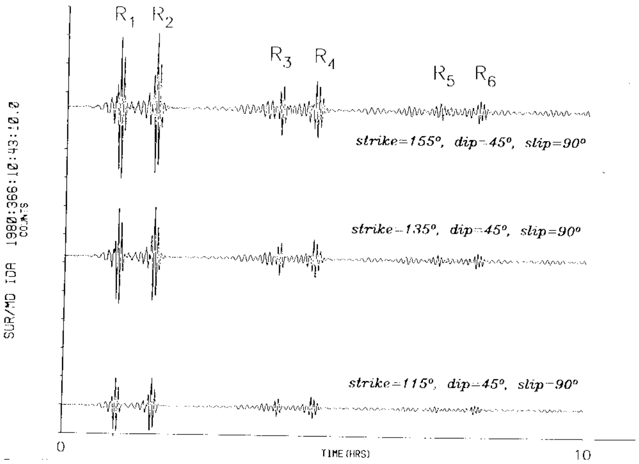

Fig. 20. First-order splitting synthetics for IDA station SUR using a thrust source offshore Oaxaca, Mexico (16°N, 96.6°W). Three choices of strike are shown, representing a 40° sweep across the lobe of the Rayleigh wave source radiation pattern. The relative amplitude anomaly of R_3 and R_4 remains unchanged, even though the absolute amplitude of the waveforms varies greatly.

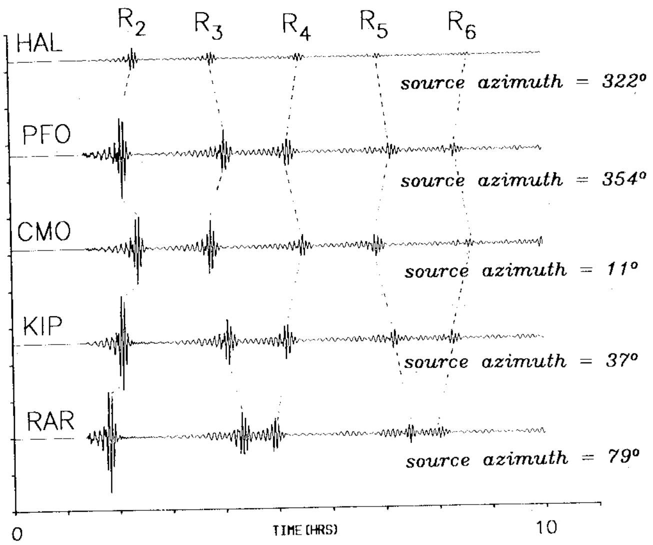

Fig. 21. Dispersion branch coupled synthetics for 1978 Tabas, Iran, event for the five IDA records shown in Figure 12. The first 10 hours are shown. R_1 has been omitted in order to facilitate comparison with the edited data traces.

were split into two groups according to whether the ratio was greater or less than unity. The rms and extremal amplitude ratios were found for each group and plotted with triangles/solid lines and circles/dotted lines, respectively. Ratios for first-order splitting relative to spherical earth synthetics are shown in Figure 27. Roughly 10% of the 76 seismogram pairs exhibit amplitude anomalies of 30% or more in R_2, R_3, and R_4, twice as many for R_5 and R_6. Isolated cases show a ratio greater than 3 or less than 0.1. There is a tendency for the rms amplitude anomaly to increase with orbit number, reaching 30% anomaly for R_5, R_6 in the higher frequencies. This behavior can be plausibly explained in terms of focusing or defocusing regions in the laterally varying structure. The focusing/defocusing effect would be enhanced each time a surface wave packet traverses the relevant anomaly.

The effect of odd-order lateral structure on amplitude anomalies can be assessed in Figure 28, where first-order splitting and dispersion branch coupled synthetics are compared. The amplitude perturbations are relatively small, with only 2 or 3 out of 76 (depending on frequency) amplitude ratios more than 30% anomalous. The rms amplitude anomalies of 5–7% were observed for $f \geq 4$ mHz, with little variation with increasing orbit number. The relatively small amplitude perturbations are a disappointment and do not coincide with the generalization that one expects from coupling calculations. If neighboring modes on a dispersion branch are coupled, frequency perturbations due to nearest neighbors tend to cancel. Amplitude variations vary as $(\Delta f)^{-1}$ and are therefore expected to be much larger than frequency perturbations, especially if the modes are widely spaced in frequency. Since nearest neighbors ($\Delta f \sim 0.1$ mHz) on the spheroidal fundamental branch are relatively widely spaced, one would expect amplitude effects to dominate. That they do not may be explained by the nearly identical spatial wavefunctions of ${}_0S_l$ free oscillations at large l. The hybrid particle motion of the coupled oscillations does not differ enough from the unperturbed particle motion to cause large variations in waveform character or amplitude.

Much interest has centered on inversions of the entire seismic waveform [e.g., *Woodhouse and Dziewonski*, 1984; *Lerner-Lam and Jordan*, 1983]. Differential seismograms are constructed from the difference between the observed seismogram and a synthetic constructed from the spherical starting model. The differential seismogram is assumed to be linearly related to a perturbation in the model. Perturbations are calculated that improve the fit between the observed seismogram and the calculated synthetic. Goodness of fit is typically assessed in terms of the variance of the differential seismogram relative to that of the starting synthetic. If $u_D(t)$ is the observed seismogram and $u_S(t)$ is the synthetic, the fractional variance of the differential seismogram $u_D - u_S$ is

$$\sum_{t=1}^{T} (u_D(t) - u_S(t))^2 \Bigg/ \left[\sum_{t=1}^{T} (u_S(t))^2 \right] \tag{20}$$

Values of this fractional variance were calculated for the 132 source-receiver pairs of Table 1 between spherical earth, first-order splitting and dispersion branch coupled synthetics, each time taking the more complicated coupling scheme as the "observed" record. The average variance generated by even-order structure in a first-order splitting synthetic totaled 15.6% that of the spherical earth synthetic. The variance caused by dispersion branch coupling relative to first-order splitting averaged 4.75%, that relative to spherical earth synthetics averaged 19.8%. Since 19.8 − 15.6 = 4.2 is not greatly different from 4.75, the waveform perturbation caused by the more extensive coupling appears on average to be orthogonal to that induced purely by even-order structure. Comparison of variance fractions by individual source-receiver pair confirm this. This demonstrates that the branch-coupled synthetics could not be fit much better by a simple amplification of the even-order lateral structure. However, it cannot be concluded from this simple exercise that

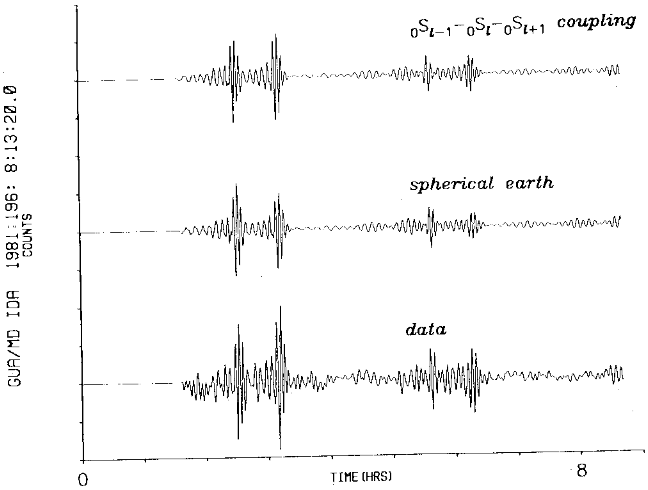

Fig. 22. Data synthetic comparison for July 15, 1981, New Hebrides event using IDA station GUA. R_1 has been omitted. The data trace is at the bottom. The central trace is the spherical earth synthetic. The top trace is the dispersion branch coupled synthetic. Note that the top trace reproduces the relative amplitude anomalies seen in the data trace.

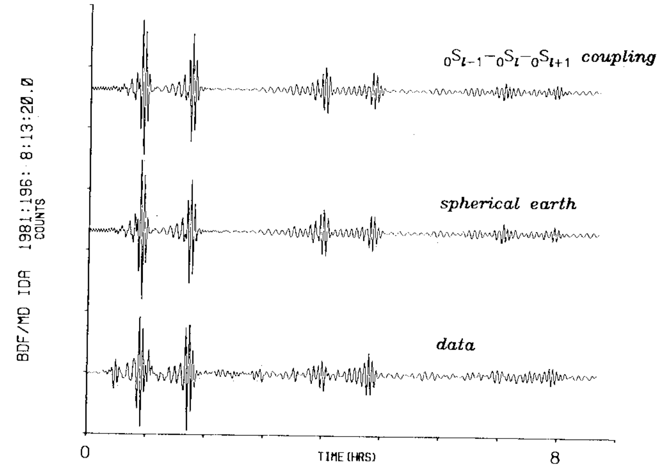

Fig. 23. Same as Figure 22, but for IDA station BDF. Note that the coupled-mode synthetic does not predict the observed R_3–R_4 amplitude reversal.

they could not be better fit by a strictly even-order model of a different shape.

If the dispersion branch coupled M84A synthetic is taken as representative of observed data, the spherical earth synthetic explains, on average, roughly 80% of the observed variance. Studies of actual data rarely are this successful, for several obvious reasons. Our numerical experiment has no noise, overtones, or instrument miscalibrations. The underlying radial earth model, including Q structure, is precisely known. Coupling to toroidal modes, whose importance will later be shown, is not included. The variance quantities here are appropriate for low-passed IDA records. Seismic response at higher frequencies will likely be more sensitive to the highly variable shallow structure in M84A. However, we take this experiment to be indicative of the effects of plausible upper mantle lateral structure on long-period fundamental Rayleigh waves. In particular, the small waveform perturbations caused by the odd-order components relative to those caused by even-order structure should inspire caution when data analysis schemes are used that attempt to measure both simultaneously. In inversion schemes that rely on reducing the overall waveform misfit variance, the odd-order structure could be masked in the misfit left over from obtaining the even-order lateral structure components.

4. EFFECT OF CORIOLIS COUPLING IN TIME DOMAIN

We have thus far considered interaction only among spheroidal fundamental modes. Much more interaction is possible, given a sufficiently heterogeneous earth model. Continent-ocean models and spherical harmonic upper mantle models like M84A cause weak intramultiplet coupling in all but isolated cases. However, rotational Coriolis force causes strong coupling between fundamental Rayleigh and Love waves in certain angular orders and frequencies. The Coriolis functional $W(\mathbf{s}^*,\mathbf{s})$ defined in (5) depends on the earth's spherically averaged density structure, which is much better known than the lateral variations in ρ, κ, and μ. The value of the Coriolis interaction can therefore be modeled to a relatively high precision. The frequency-domain behavior of Coriolis force is discussed by *Masters et al.* [1983*a*]. In the time domain, Coriolis force can cause visible waveform anomalies that complicate a traveling wave interpretation of a long-period seismogram.

Four synthetic records for IDA station ESK are shown in Figure 29. A strike-slip source with 0° strike was used at the hypocenter of the June 22, 1977, Tonga event. The lower three traces show well-formed wave packet arrivals. The amplitude of the first-order splitting trace is slightly enhanced relative to the spherical earth control synthetic, while a noticeable odd-even enhancement exists in the dispersion branch coupled case. The upper trace shows a synthetic constructed from coupled spheroidal and toroidal fundamentals using ellipticity, rotation, and model M84A. Although wave packets R_1 through R_6 are still discernible, the waveforms are disrupted by precursory energy. This energy is well-dispersed with only slightly variable frequency but arrives roughly at the Love wave group velocity (about 4.44 km/s at $f = 4$ mHz). The nominal arrival times of G_1 through G_6 are indicated. This precursory energy, which we term a low-frequency quasi-Love wave, is quite unexpected: ordinary Love waves, composed of toroidal modes, do not possess a vertical component. Coriolis coupling, principally between the pairs $_0S_l-_0T_{l+1}$, $9 \leq l \leq 22$ and $_0S_l-_0T_{l-1}$, $30 \leq l \leq 34$, creates hybrid toroidal modes that possess a significant spheroidal component and hence possess vertical motion. One therefore expects quasi-Love waves to exist at periods $T \gtrsim 240$ s. Since coupling is not uniform over frequency, the observed wave is highly dispersed, lacking the pulselike appearance of ordinary Love wave arrivals. Quasi-Love waves will also appear on the radial component of horizontal component seismograms. A complementary effect will cause the contamination of the transverse horizontal component record with wave motion at the Rayleigh arrival times.

The size of these precursory waveforms should cause concern for future investigations of deep earth structure. Happily, the presence or absence of quasi-Love energy is dependent on source mechanism and source-receiver path

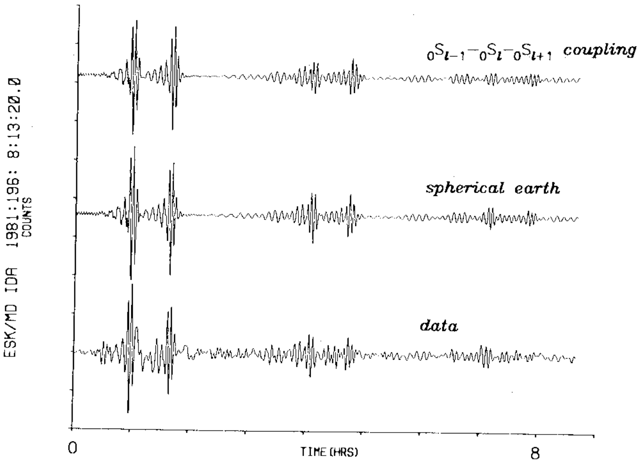

Fig. 24. Same as Figure 22, but for IDA station ESK. In this example the coupled-mode synthetic predicts an amplitude anomaly not seen in the data record.

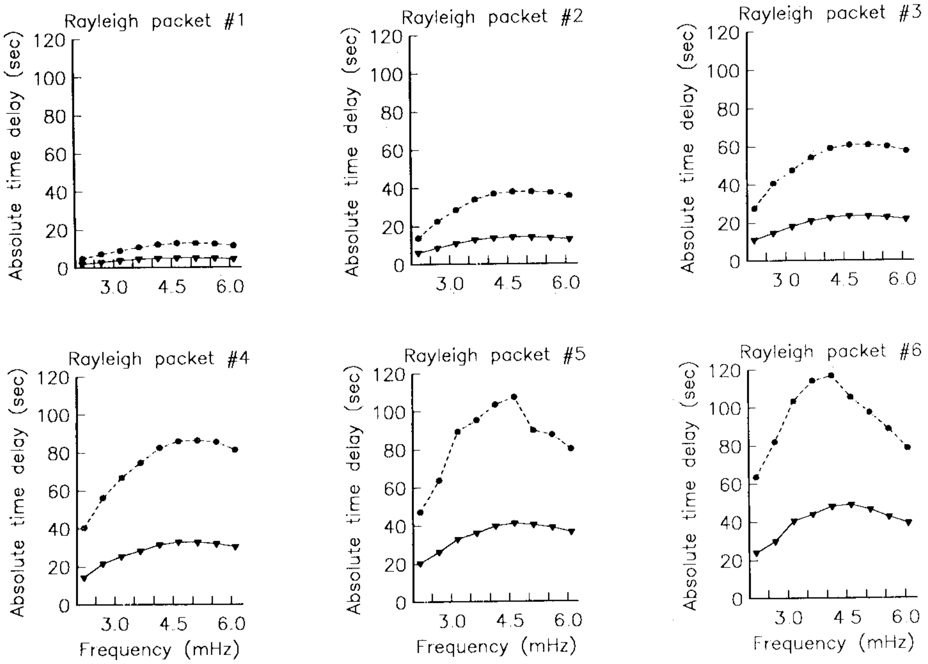

Fig. 25. The rms average and maximum absolute time delays for 76 source-receiver pairs of first-order splitting synthetics relative to spherical earth synthetics. Results for R_n, $n = 1,\ldots,6$, are shown versus cycle frequency. Maximum absolute time shifts are plotted with circles and connected with dashed lines. The rms average absolute time delays are plotted with triangles and connected with solid lines. Note how the average time delay grows with wave packet order, as the great circle time delays accumulate in successive orbits.

in a predictable manner. The Coriolis force couples ${}_0S_l - {}_0T_{l\pm 1}$ multiplet pairs so that only singlets with identical azimuthal order m interact. This behavior derives from the independence of Coriolis force with longitude. The size of the interaction among these singlet pairs varies with azimuthal order as $\sqrt{\bar{l}^2-m^2}$, where $\bar{l}$ is the larger angular order of the two multiplets. Interaction is maximal for $0 \approx |m| << \bar{l}$ and minimal for $|m| \approx \bar{l}$. Consider the asymptotic regime $l >> 1$. If the pole of the great circle connecting source and receiver lies at latitude Θ, the recorded seismic signal will consist principally of singlets whose azimuthal orders satisfy $\cos\Theta \approx m/(l+\frac{1}{2})$. There-

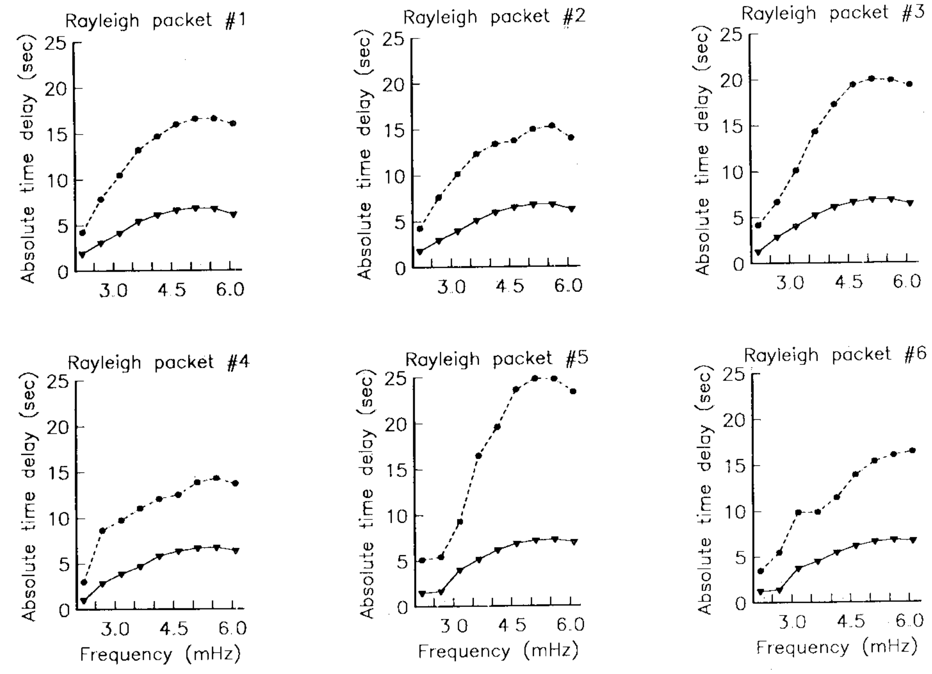

Fig. 26. Same as Figure 25, but showing comparison of absolute time delays of dispersion branch coupled synthetics (sensitive to all structure) relative to first-order splitting synthetic (sensitive to even structure only). Note that the rms time delay remains virtually constant with increasing order number.

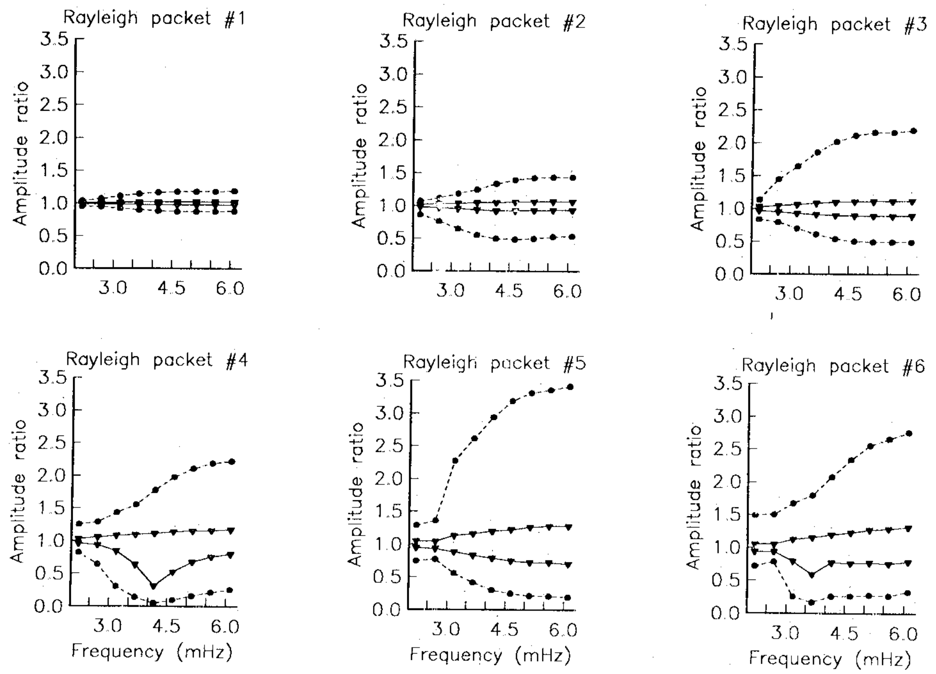

Fig. 27. Maximum and rms average amplitude ratios for 76 IDA source-receiver pairs, comparing first-order splitting with spherical earth synthetics. Two sets of measurements are plotted for each R_n, $n = 1, \ldots, 6$, one set for coupled-mode wave packets that have excess amplitude, the second for coupled-mode wave packets that have deficient amplitude. Maximum amplitude anomalies are plotted versus frequency with circles connected by dotted lines. The rms average amplitude ratios are plotted with triangles connected by solid lines. The rms amplitude ratio increases overall with order number, but not uniformly.

fore we expect rotationally coupled quasi-Love waves to be observed more often on polar $(\Theta \approx 90^\circ)$ propagation paths than on equatorial $(\Theta \approx 0^\circ)$ propagation paths. For example, the great circle pole of the Tonga-ESK example of Figure 29 lies at 83° colatitude. A hueristic mnemonic for this behavior can be scavenged from an undergraduate physics example. Coriolis deflection is felt strongly by an airplane flying over one of the earth's poles, as the earth changes orientation under the plane. On a flight path along the equator, the earth's rotation changes the

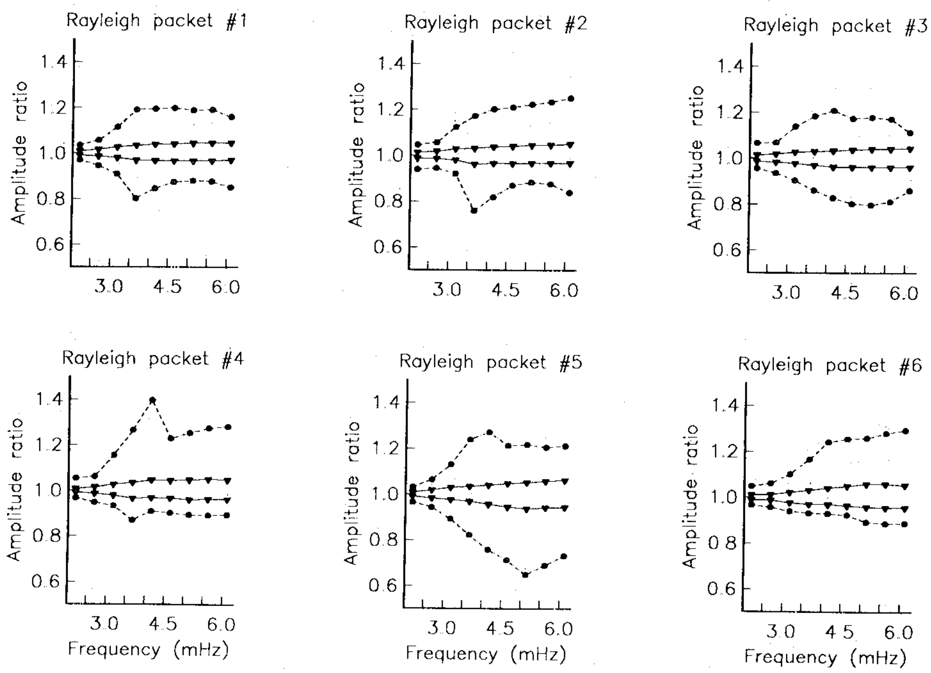

Fig. 28. Same as Figure 27, but showing comparison of amplitude ratios of dispersion branch coupled synthetics relative to first-order splitting synthetics. The measured anomalies are more modest than those in the previous figure and do not show a strong trend with increasing wave packet order.

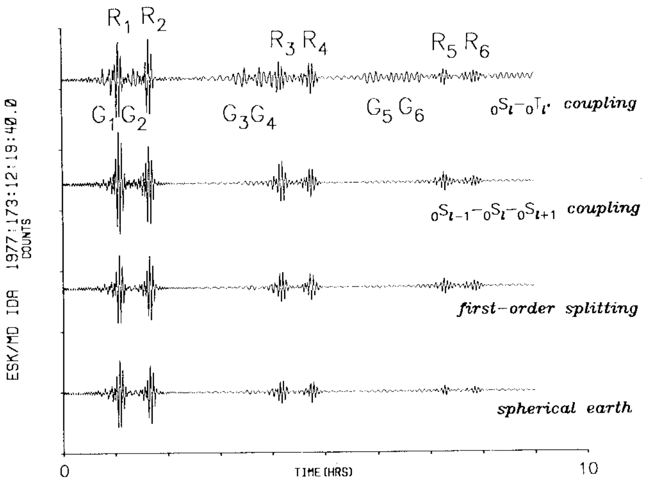

Fig. 29. Comparison of coupling schemes for IDA station ESK record using a synthetic source at the hypocenter of the 1977 Tonga event. The lower three traces show spherical earth, first-order splitting, and dispersion branch coupled synthetics, none of which include the effects of coupling of spheroidal and toroidal motion. The top trace includes coupling effects between fundamental spheroidal and toroidal modes. Rayleigh wave packets R_n, $n = 1,\ldots,6$, are indicated, as are the arrival times of Love wave packets G_n, $n = 1,\ldots,6$, nominally devoid of vertical component motion.

airplane's speed with respect to the ground from that observed in an inertial frame of reference but does not vary its orientation with respect to the ground. The same rules apply to seismic particle motion. Along the equator, the propagation speed of particle motion will be perturbed (and hence give rise to rotational self-splitting) but the motion will not be deflected. Deflection of particle motion increases, however, as the propagation path inclines toward the polar regions, thereby enhancing the conversion of spheroidal to toroidal motion, and vice versa.

Since the quasi-Love precursor is the vertical component rider to the main Love wave, it is most likely to be observed where long-period Love waves are strongly excited. This criterion favors strike-slip mechanisms as observational candidates. Since Love wave nodes and antinodes in the source radiation pattern coincide with Rayleigh wave antinodes and nodes, respectively, we expect the relative prominence of quasi-Love motion to vary greatly with source strike (for a collection of events at a given location and one station) and source azimuth (for a collection of stations and one event). Two examples using a strike-slip mechanism at the Tonga hypocenter are shown in Figures 30 and 31. In the first, IDA response at NNA is modeled using coupled spheroidal and toroidal fundamentals for five mechanisms with fault strike varying between 60° and 100°. $\Theta = 27°$ for this source-receiver pair, dominantly an equatorial path. The Rayleigh wave packets vary in amplitude as the Rayleigh radiation lobe passes from antinode to node, but no quasi-Love motion is evident. Figure 31 shows results for near-polar ($\Theta = 83°$) source-receiver pair Tonga-ALE, using strikes from 50° to 90°. At 50° strike the Love wave node at Tonga is directed toward ALE, and the waveforms are not visibly perturbed. However, as the Love wave antinode rotates toward the source-receiver azimuth (−7.6°), quasi-Love precursors invade the seismogram. At 80° and 90° strike, R_3 and R_4 have drowned in a long train of greatly dispersed oscillatory motion.

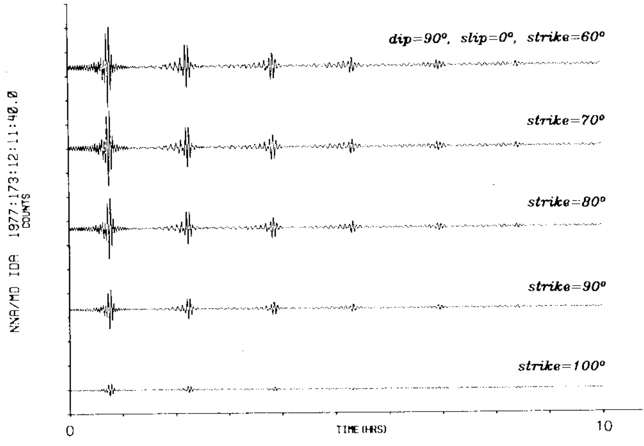

Fig. 30. The ${}_0S_l-{}_0T_{l'}$ synthetics for IDA station NNA using strike-slip sources at the hypocenter of the 1977 Tonga event. The choices of source strike sweep roughly from Rayleigh wave radiation node to the Rayleigh wave radiation antinode.

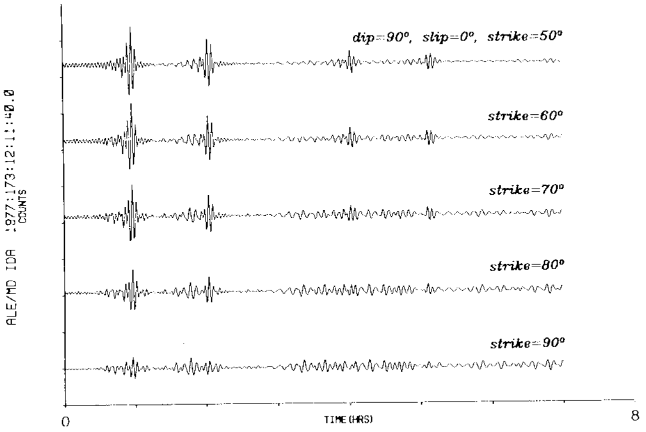

Fig. 31. Same as Figure 30, but for IDA station ALE. The source-receiver great circle is nearly polar for this example. As the source strike sweeps to align the Rayleigh source radiation node with the source-receiver great circle, coupled mode effects dominate the seismic record.

Clear examples of quasi-Love waves in IDA data are not common. Favorable source-receiver orientation is necessary, with a lobe of the Love wave radiation pattern pointing north-south and a hypocenter shallow enough not to excite significant overtone amplitudes. We show data versus synthetic examples from a September 12, 1979, event in western New Guinea (1.7°S, 136.7°E). We use a moment tensor derived by *Masters et al.* [1983*b*] using seven IDA and GDSN records and spherical earth Green's functions: $M_0 = 2.1 \times 10^{27}$ dyne cm, $\mathbf{m} = (0.05, 0.78, -0.83, -0.29, -0.14, 1.91) \times 10^{26}$ dyne cm, dominantly strike-slip with fault and auxiliary planes aligned at 15.1° and 105.7° strike, measured clockwise from north. The apparent depth of focus was 5 km, which argues against overtones being a large contributing factor.

We compare data with mixed-mode and first-order splitting synthetics for station KIP (Kipahpa, Hawaii) in Figure

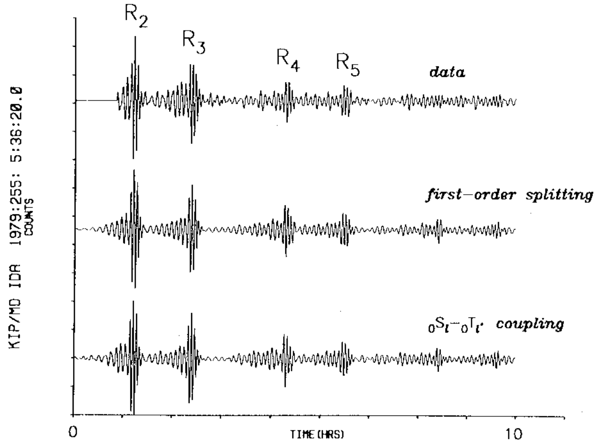

Fig. 32. Data-synthetic comparison for 1979 New Guinea event at IDA station KIP. The bottom trace is the mixed-mode synthetic. The top trace is data from the event. The middle trace is the first-order splitting synthetic. The IDA gravimeter resonse to R_1 was nonlinear and so was omitted. No mixed-mode coupling effects are observed in the traces, owing to the high latitude ($\Theta = 23.9°$) of the pole of the source-receiver great circle.

32. The great circle pole for this propagation path lies at colatitude $\Theta = 23.9°$. The great circle connecting source and receiver exits the source within 6° of the Rayleigh radiation antinode, quite unfavorable for quasi-Love observations. No anomalous behavior is evident in either data or synthetics. The qualitative fit between the low-passed data waveform and that of the two synthetics demonstrates the absence of overtone waves, which would arrive between the Rayleigh wave packets. IDA station TWO (Figure 33) demonstrates a polar ($\Theta = 86.2°$) propagation path that exits the source 18° away from the Rayleigh radiation node. A large precursor to R_2 and an entire long-period wave packet between R_3 and R_4 are absent in the first-order splitting synthetic but can be seen as quasi-Love arrivals in the mixed-mode synthetic. The additional quasi-Love anomaly after R_5 is a likely explanation for similar long-period motion after R_5 in the data. The precise fit of the anomalous waveforms is not good, but it must be remembered that the amount and distribution of coupling is heavily dependent on the relative frequency spacing between the spheroidal and toroidal fundamental mode branches. The results of *Masters et al.* [1983*a*] suggest that this spacing is not adequately modeled in model 1066A or any other current standard model. The group velocity match between waveforms, as well as the visible low-frequency content, argue for Coriolis coupling as the principal cause. Another near-polar path ($\Theta = 65.6°$) is available from station CMO (Figure 34). The great circle for this station intersects the source within 10° of the Rayleigh wave radiation node. The qualitative fit in this example is poor beyond R_3, but strong precursors to R_2 and R_3 have their counterparts in the mixed-mode synthetic. Our ability to model better these seismic records will hinge on better representation of mixed-mode coupling, which will depend critically on future improvements to radial earth models.

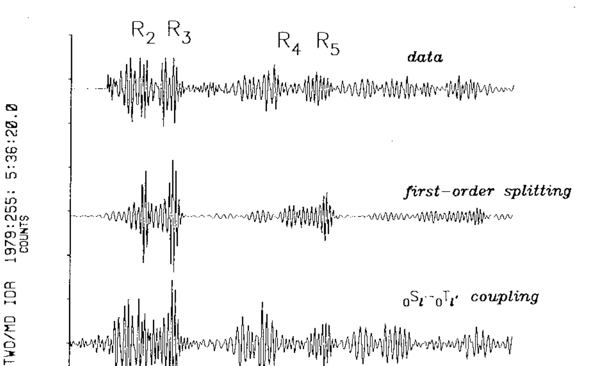

Fig. 33. Same as Figure 32, but for IDA station TWO. Strong mixed-mode coupling effects are seen in the top and bottom traces for this near-polar ($\Theta = 86.2°$) propagation path.

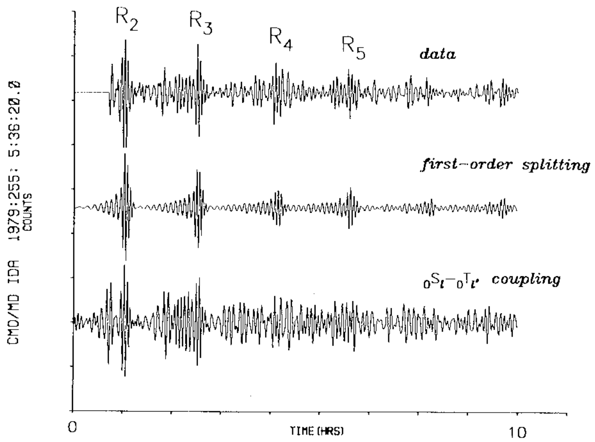

Fig. 34. Same as Figure 32, but for IDA station CMO. Strong mixed-mode coupling effects are seen in the top and bottom traces for this high latitude ($\Theta = 65.6°$) propagation path.

The problems caused by our imprecise knowledge of the relative placement of spheroidal and toroidal fundamental mode branches are clearly demonstrated in a comparison of the spectra of the seismic records shown in Figures 33 and 34. Amplitude spectra for data and synthetics of IDA station TWO are shown in Figure 35. The spectra are normalized to instrument count units for easy comparison of the y ordinate. The data spectrum is dominated by spectral peaks at frequencies corresponding to the spheroidal fundamental modes $_0S_l$, with relatively little spectral amplitude at overtone frequencies. The amplitudes of the fundamentals vary in an irregular pattern, unlike the smooth "rolls" evident in the first-order splitting synthetic. This band encompasses Coriolis coupling pairs $_0S_l-_0T_{l+1}$, $12 \leqslant l \leqslant 19$. The degenerate frequency for $_0S_{19}$ (2.776 mHz) is prominently anomalous in both spectra and is marked with an asterisk. One of the $_0S_l-_0T_{l+1}$ dispersion branch crossings occurs between $_0S_{18}$ and $_0S_{19}$ in all current radial earth models, e.g., PREM, 1066A. The $_0S_l-_0T_{l-1}$ mode branch crossing, common to all current models, occurs at $l = 32$ (3.993 mHz) and is indicated by a second asterisk. *Masters et al.* [1983*a*] show that this crossing is misplaced, perhaps by 30 μHz or more. The enhanced amplitudes seen in the mixed-mode synthetic spectrum match the data amplitudes poorly near this frequency.

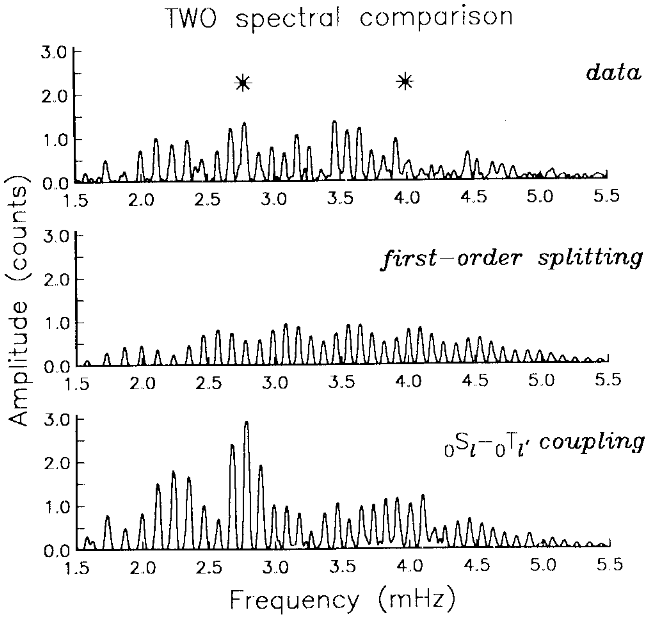

Fig. 35. Spectra of the seismic traces shown in Figure 33. The asterisks mark the degenerate frequencies of the modes $_0S_{19}$ (2.776 mHz) and $_0S_{32}$ (3.993 mHz). Note the predominance of fundamental mode energy in the data spectrum.

Figure 36 shows spectral for the CMO records shown in Figure 34. Asterisks mark the degenerate frequencies of $_0S_{18}$ (2.672 mHz) and $_0S_{32}$. The data spectrum is dominated by fundamental mode spectral peaks in an irregular amplitude pattern. Note, however, that in the 3.0–3.6 mHz and 4.6–5.5 mHz frequency bands, where predicted Coriolis coupling is weak, the peak amplitudes mimic the alternating pattern of the first-order splitting synthetic. Both data and mixed-mode synthetic are anomalous in the 1.8–2.9 mHz frequency band, corresponding to $_0S_l-_0T_{l+1}$ coupling pairs with $11 \leqslant l \leqslant 20$. Anomalous amplitudes are evident near the mode branch crossing at $f = 3.993$ mHz also, but the amplitude of the peak at the crossing is seriously overpredicted by the mixed-mode synthetic. The suspected misplacemnt of this dispersion branch crossing in model 1066A may be at fault.

These examples suggest that a quantitative waveform comparison of mixed-mode synthetic seismograms and data is premature, given the need for a more accurate spherical earth model as the starting point in coupling calculations. The existence of anomalous waveforms due to mixed-mode Coriolis coupling can be established by a qualitative comparison of Figures 32–36.

The pitfalls of interpreting the above waveforms without reference to Coriolis coupling effects should not be minimized. In a waveform inversion scheme that only considers perturbations to Rayleigh and Love waves separately, the quasi-Love precursor will remain unmodeled. Any attempt to improve variance reduction in the waveform by fitting the quasi-Love precursor will lead to bias. If more direct measurements of phase and amplitude perturbations are taken, the chances for bias are no less. To demonstrate this, we correlated the 70° strike Tonga-ALE seismic trace from Figure 31 and performed a correlation analysis with a corresponding first-order splitting synthetic. The mixed-mode synthetic has visible quasi-Love waveforms, yet the Rayleigh wave packets are easily discernible. Amplitude ratios are graphed for R_2 and R_3 in Figure 37. As before, 1-hour time windows about the R_n arrival times are taken for spectral analysis. The overall behavior differs greatly from that common to the coupled-mode comparisons reported earlier. Large variation in amplitude is found at $f < 3.5$ mHz with little discrepancy at higher frequencies, reversing the usual pat-

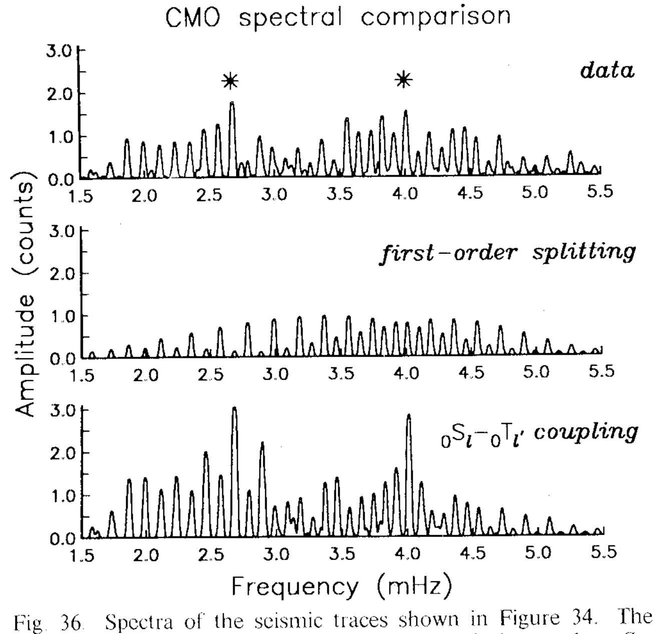

Fig. 36. Spectra of the seismic traces shown in Figure 34. The asterisks mark the degenerate frequencies of the modes $_0S_{18}$ (2.672 mHz) and $_0S_{32}$ (3.993 mHz). Note the predominance of fundamental mode energy in the data spectrum.

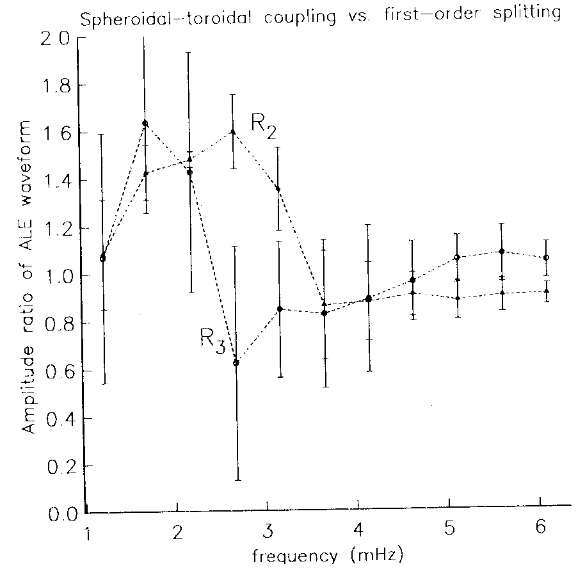

Fig. 37. Amplitude ratio measurements for mixed-mode synthetic versus first-order splitting synthetic using source-receiver geometry of Figure 31. The strike-slip source with 70° strike (middle trace of Figure 35) was used. Measured ratios for R_2 and R_3 are highly variable for $f \leqslant 4.5$ mHz, with large uncertainties. This behavior is caused by mixed-mode coupling bias.

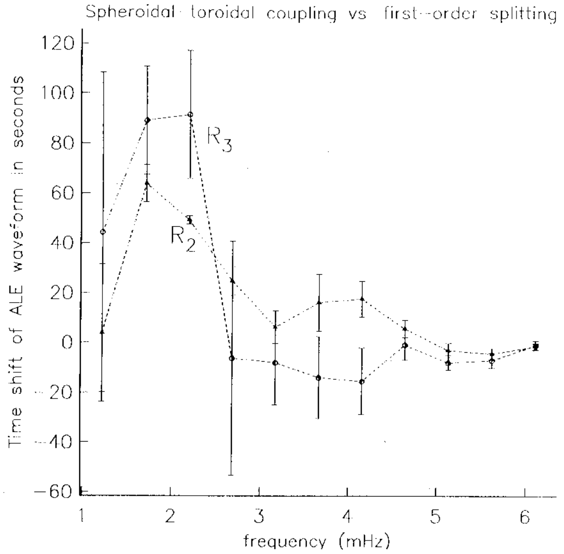

Fig. 38. Measured time shift of waveform versus cycle frequency using the synthetic comparison pair used in Figure 35. Note the large uncertainties and large variability of time delay measurements of R_2, R_3 for $f \lesssim 4.5$ mHz.

tern. Moreover, the large uncertainties returned by the correlation analysis at $f \lesssim 4.5$ mHz show that the phase match between waveforms is poor at low frequencies. Time delay measurements between R_2 and R_3 (Figure 38) show considerable bias at low frequencies as well. Measurements of $\Delta t > 50$ s dwarf the typical Δt found between first-order splitting and dispersion branch coupled synthetics. Moreover, the positive time delays reported by the correlation analysis are actually large negative time delays aliased by some multiple of the oscillation period, since the principal perturbation is the addition of a precursory waveform.

The existence of mixed-mode coupling at low frequencies will complicate the detection of lateral structure using global surface wave inversions. Coriolis coupling effects may force researchers to discard data from many source-receiver pairs at periods $T > 225$ s, thereby decreasing the possible resolution of structure in the mantle. Love wave observations will likewise be contaminated by quasi-Rayleigh waves caused by the toroidal components of hybrid spheroidal multiplets. The poorer low-frequency response of three-component GDSN instruments renders these reciprocal mixed-mode effects less visible, but no less extant. The azimuthal dependence of Coriolis effects may bias studies of Rayleigh and Love wave anisotropy at low frequencies. Coriolis coupling dies out at $f > 4.1$ mHz, after the ${}_0S_{32}-{}_0T_{31}$ crossover. Structure-dependent mixed-mode effects may be significant at higher frequencies in the fundamental mode dispersion branches, thereby complicating the detection of lateral structure in the upper reaches of the mantle. Perturbations to average multiplet frequencies in data stacking and stripping suggest the existence of spheroidal-toroidal coupling at most of the ${}_0S_l-{}_0T_{l\pm\Delta l}$ dispersion branch crossovers (G. Masters and F. Gilbert, personal communication, 1985). The anisotropic lateral models proposed by *Tanimoto and Anderson* [1985] are likely to cause significant deflections of surface wave particle motion that would cause Love-Rayleigh coupling. If lateral structure of scale length $\lesssim 4000$ km varies strongly with radius, significant coupling between fundamental and overtone branches is possible as well. Adequate modeling of such effects, however, will require lateral structure models with rougher variation than that of M84A or Nakanishi and Anderson's spherical harmonic models, as the Δl between coupling candidates ${}_0S_l$, ${}_nS_{l'}$ can easily be 10 or greater.

5. CONCLUSIONS

Synthetic seismograms that are constructed from coupled free oscillations offer the most precise method currently available to model the effects of lateral structure in low-frequency seismic records. They offer a useful check on traveling wave and tomographic approximations to surface wave behavior. Since these approximations yield tractable inverse problems for aspherical structure in the upper mantle, forward modeling with free oscillations is important to assess any possible bias. Evidence for sensitivity to structures that lie off the great circle connecting source and receiver is common in the synthetics. For a continent ocean model consistent with that proposed by *Sipkin and Jordan* [1976, 1980], we find deflections of wave packet arrival azimuth of up to ~10° away from the great circle azimuth. $R_{n+2}-R_n$ great circle transmit times vary up to 10 s at 4–6 mHz depending on the orbit and can show a trend in frequency where the tomographic approximation predicts none.

We have used model M84A of *Woodhouse and Dziewonski* [1984] in a suite of numerical tests. We expect that seismograms calculated for the lateral structure models of *Nakanishi and Anderson* [1983, 1984] will behave in a similar manner. Many surface wave amplitude anomalies are noticeable in the synthetics. Roughly 10% of 76 modeled source receiver pairs showed amplitude anomalies of 30% or more, with isolated cases whose amplitudes varied by a factor of 3 or more. These anomalies were observed, using spectral correlation methods, to increase with frequency. Amplitude anomalies are interpreted in terms of focusing and defocusing effects of lateral structures, producing an alternating amplitude with successive Rayleigh wave packets that is observed in data and has been produced by the lateral ray-tracing schemes of *Lay and Kanamori* [1985] and by *Wong and Woodhouse* [1983]. In one case the coupled-mode synthetics produce an anomaly pattern that reverses sense as the strike of the source mechanism sweeps across the great circle connecting source and receiver. Although model M84A generates a plethora of amplitude anomalies, its fit to observed anomalies from the 1978 Tabas, Iran, event and a set of 1981 New Hebrides events is not good.

We compared the effects of the even- and odd-order structures of M84A by constructing synthetic seismograms using the full model ($s \leqslant 8$) and only its even part. The misfit variance relative to spherical earth synthetics averaged 15.6% for synthetics sensitive to even-order structure only. Odd-order structure caused an additional 4–5% variance misfit on average. Phase shifts and amplitude anomalies associated with purely even-order structure tend to increase with successive Rayleigh packet orbit, while the incremental anomalies associated with odd-order structure were essentially constant. This behavior is consistent with the assumptions underlying the tomographic major arc/minor arc method of separating even- and odd-order structural effects. Large wave packet amplitude anomalies are only slightly more common in synthetics sensitive to all structure compared to those sensitive to even structure.

Coriolis coupling between spheroidal and toroidal oscillations is visible in some seismic records. This behavior manifests itself on vertical component records in the form of quasi-Love precursors to Rayleigh wave packets, caused by the spheroidal component of a dominantly toroidal (Love) wave motion. Quasi-Love precursors are long period ($T \gtrsim 240$ s) and are well dispersed. Theoretical considerations predict that this effect is maximal on polar source-receiver paths when the Love wave radiation antinodes point north-south. Synthetic experiments confirm this. Even at source-receiver orientations that are not optimal for the generation of quasi-Love precursors, their presence can seriously bias measurements of frequency-dependent phase shift and amplitude.

The scope of this study is not adequate to provide a thorough critique of lateral structure models like M84A. However, some cautions should be noted in future studies of earth lateral structure with surface waves. If the upper mantle is as heterogeneous as model M84A, there will be significant departures from the assumption that measured data depend only on structure directly beneath the great circle connecting source and receiver. How much these departures bias a model obtained using these tomographic assumptions is not yet known and must await a more complete study. At low frequencies the occasional contamination by coupled spheroidal-toroidal motion is of some concern. The data and synthetic IDA records show the potential for biased measurements. These problems will be compounded for low-frequency Love wave observations contaminated by "quasi-Rayleigh" motion, the toroidal component of a dominantly spheroidal hybrid Rayleigh wave. Since spheroidal motion is less attenuative than toroidal, the hybrid Rayleigh motion will decay more slowly with time and will be relatively more prominent. Long-wavelength ($s \leq 10$) isotropic lateral structure does not efficiently couple spheroidal and toroidal motion [*Park*, 1985], so that, for models of that type, we do not expect significant contamination by mixed-mode coupling for $f \gtrsim 4.2$ mHz. However, the perturbative effects of anisotropy on seismic wave polarization are well known, and such polarization effects may significantly couple spheroidal and toroidal motion. Visible coupling effects may prove to be important evidence in determining the existence and extent of upper mantle anisotropy but may also seriously impede attempts, like that of *Tanimoto and Anderson* [1985], to measure it using directionally dependent surface wave propagation velocities.

Numerical descriptions of such extensive coupling effects are only now becoming feasible, with the availability of large supercomputers like the CRAY-1. As seismic investigations of the earths' interior reach the precision where such coupling is important in the frequency range accessible to free oscillation modeling, large coupling calculations involving several hundred singlets become necessary for proper representation of the seismic waveform. The results of this study suggest that this point has already been reached. Future refinements of technique and expansions of computing power will allow a better understanding of low-frequency source mechanisms and three-dimensional earth structure.

Acknowledgments. Freeman Gilbert and Guy Masters offered useful help and advice during the course of this study. A large data base of edited IDA records, compiled by Guy Masters for an earlier project, proved very helpful in finding examples of the wave propagation effects discussed in this study. I also acknowledge R. C. Y. Chin, L. Thigpen, and G. W. Hedstrom for logistical help at the MFECC computing center at Livermore. The graphics routine PLOTXY, written by Robert L. Parker and Loren Shure, proved invaluable. I also thank two anonymous reviewers, who directed my attention to arguments that needed clarification. This work has been supported by National Science Foundation grants EAR-82-18612 and EAR-84-09612 and by IGPP-Lawrence Livermore National Laboratory grant PC831003.

REFERENCES

Chin, R. C. Y., Wave propagation in viscoelastic media, in *Physics of the Earth's Interior, Proceedings of the Enrico Fermi Intrnational School of Physics*, A. Dziewonski and E. Boschi, eds., Academic Press, New York, 1980.

Dahlen, F. A., Elastic dislocation theory for self-gravitating elastic configuration with an initial static stress field, II, Energy release, *Geophys. J. R. Astron. Soc., 31*, 469–484, 1973.

Dahlen, F. A., The spectra of unresolved split normal model multiplets, *Geophys. J. R. Astron. Soc., 58*, 1–33, 1979.

Dahlen, F. A., The free oscillations of an anelastic aspherical earth, *Geophys. J. R. Astron. Soc., 66*, 1–22, 1981.

Dziewonski, A. M., and J. H. Woodhouse, An experiment in systematic study of global seismicity: Centroid-movement tensor solutions for 201 moderate and large earthquakes of 1981, *J. Geophys. Res., 88*, 3247–3271, 1983.

Edmonds, A. R., *Angular Momentum in Quantum Mechanics*, Princeton University Press, Princeton, N.J., 1960.

Jordan, T. H., A procedure for estimating lateral variations from low-frequency eigenspectra data, *Geophys. J. R. Astron. Soc., 52*, 441–455, 1978.

Jordan T. H., Global tectonic regionalizations for seismological data analysis, *Bull. Seismol. Soc. Am., 71*, 1131–1141, 1981.

Lay, T., and H. Kamamori, Geometric effects of global lateral heterogeneity on long-period surface wave propagation, *J. Geophys. Res., 90*, 605–622, 1985.

Lerner-Lam, A. L., and T. H. Jordan, Earth structure from fundamental and higher-mode waveforms analysis, *Geophys. J. R. Astron. Soc., 75*, 759–798, 1983.

Luh, P. C., The normal modes of the rotating self-gravitating inhomogeneous earth, *Geophys. J. R. Astron. Soc., 38*, 187–224, 1974.

Masters, G., T. H. Jordan, P. G. Silver, and F. Gilbert, Aspherical earth structure from fundamental spheroidal-mode data, *Nature, 298*, 609–613, 1982.

Masters, G., J. Park, and F. Gilbert, Observations of coupled spheroidal and toroidal modes, *J. Geophys. Res., 88*, 10285–10298, 1983*a*.

Masters, G., K. Priestley, and F. Gilbert, Source mechanism retrieval from long-period digital data (abstract), *Eos Trans. AGU, 64*, 774, 1983*b*.

Minster, J. B., Transient and impulse responses of a one-dimensional linearly attenuating medium, I, Analytical results, *Geophys. J. R. Astron. Soc., 52*, 479–502, 1978a.

Minster, J. B., Transient and impulse responses of a one-dimensional linearly attenuating medium, II, A parametric study, *Geophys. J. R. Astron. Soc., 52*, 503–524, 1978b.

Nakanishi, I., and D. L. Anderson, Measurements of mantle wave velocities and inversion for lateral heterogeneity and anisotropy, I, Analysis of great-circle phase velocities, *J. Geophys. Res., 88*, 10–267, 1983.

Nakanishi, I., and D. L. Anderson, Measurements of mantle wave velocities and inversion for lateral heterogeneity and anisotropy, II, Analysis by the single station method, *Geophys. J. R. Astron. Soc., 78*, 573–617, 1984.

Niazi, M., and H. Kanamori, Source parameters of 1978 Tabas and 1979 Qainat, Iran: Earthquakes from long period surface waves, *Bull. Seismol. Soc. Am., 71*, 1201–1213, 1981.

Park, J., and F. Gilbert, Coupled free oscillations of an aspherical dissipative rotating earth: Galerkin theory, *J. Geophys. Res.* (in press).

Park, J., An application of Galerkin theory to the coupling of the earth's free oscillations, Ph.D. thesis, Univ. of Calif., San Diego, La Jolla, 1985.

Sipkin, S. A., and T. H. Jordan, Lateral heterogeneity of the upper mantle determined from travel times of multiple *ScS*, *J. Geophys. Res., 81*, 6307–6320, 1976.

Sipkin, S. A., and T. H. Jordan, Multiple *ScS* travel times in the western Pacific: Implications for mantle heterogeneity, *J. Geophys. Res., 85*, 853–861, 1980.

Slepian, D., Some comments on Fourier analysis, uncertainty and modeling, *SIAM Rev., 25*, 379–393, 1983.

Tanimoto, T., and D. L. Anderson, Lateral heterogeneity and azimuthal anisotropy of the upper mantle 100–200 s, *J. Geophys. Res., 90*, 1842–1858, 1985.

Tanimoto, T., and B. A. Bolt, Coupling of torsional modes in the earth, *Geophys. J. R. Astron. Soc., 74*, 83–96, 1983.

Thomson, D. J., Spectrum estimation and harmonic analysis, *Proc. IEEE, 70*, 1055–1096, 1982.

Wong, Y. K., and J. H. Woodhouse, Ray theory for surface waves on a sphere (abstract), *Eos Trans. AGU, 64*, 260, 1983.

Woodhouse, J. H., On Rayleigh's principle, *Geophys. J. R. Astron. Soc., 46*, 11–22, 1976.

Woodhouse, J. H., The coupling and attenuation of nearly resonant multiplets in the earth's free oscillation spectrum, *Geophys. J. R. Astron. Soc., 61*, 261–283, 1980.

Woodhouse, J. H., and F. A. Dahlen, The effect of a general aspherical perturbation on the free oscillations of the earth, *Geophys. J. R. Astron. Soc., 53*, 335–354, 1978.

Woodhouse, J. H., and A. M. Dziewonski, Mapping of the upper mantle: Three-dimensional modeling of earth structure by inversion of seismic waveforms, *J. Geophys. Res., 89*, 5953–5986, 1984.

Woodhouse, J. H., and T. P. Girnius, Surface waves and free oscillations in a regionalized earth model, *Geophys. J. R. Astron. Soc., 68*, 653–673, 1982.

J. Park, Geophysical Fluid Dynamics Program, Princeton University, P.O.Box 308, Princeton, NJ 08540.

(Received March 29, 1985;
revised September 9, 1985;
accepted December 3, 1985.)